

www.acsami.org Research Article

Fabrication and Characterization of Zn Particle Incorporated Fibrous Scaffolds for Potential Application in Tissue Healing and Regeneration

Felix Tettey, [∇] Sheikh Saudi, [∇] Dekonti Davies, Sita Shrestha, Kalene Johnson, Svitlana Fialkova, Kiran Subedi, Bishnu P. Bastakoti, Jagannathan Sankar, Salil Desai, and Narayan Bhattarai*



Cite This: https://doi.org/10.1021/acsami.3c09793



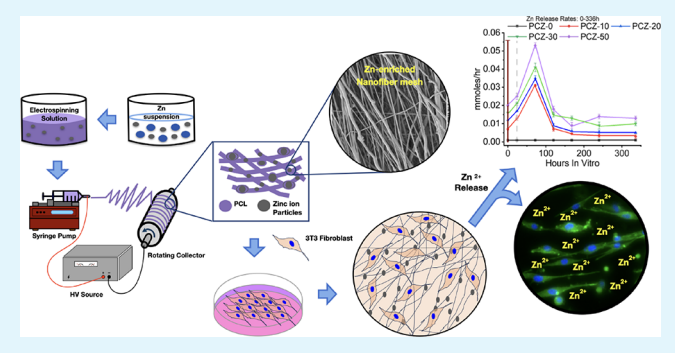
ACCESS

III Metrics & More

Article Recommendations

s Supporting Information

ABSTRACT: Zinc (Zn) metal and its alloys have received a lot of interest in biomedical applications due to their biodegradability, biocompatibility, antimicrobial activity, and ability to stimulate tissue regeneration. Bulk Zn has been successfully utilized in a variety of implant applications, most notably as bioabsorbable cardiac stents and orthopedic fixation devices, where it provides adequate mechanical properties while also releasing helpful Zn ions (Zn²+) during degradation. Such beneficial ions are dosedependent and, when released in excess, can induce cellular toxicity. In this study, we hypothesize that embedding Zn metal particles into a polymer nanofibrous scaffold will enable control of the degradation and time release of the Zn²+. We designed and



fabricated two polymer scaffolds, polycaprolactone (PCL) and polycaprolactone-chitosan (PCL-CH). Each scaffold had an increasing amount of Zn. Several physicochemical properties such as fiber morphology, crystallinity, mechanical strength, hydrophilicity, degradation and release of Zn²⁺, thermal properties, chemical compositions, and so forth were characterized and compared with the PCL fibrous scaffold. The biological properties of the scaffolds were evaluated in vitro utilizing direct and indirect cytotoxicity assays and cell viability. All the data show that the addition of Zn changed various physical properties of the PCL and PCL-CH scaffolds except their chemical structure. Further investigation reveals that the PCL-CH scaffolds degrade the Zn particles relatively faster than the PCL because the presence of the hydrophilic CH influences the faster release of Zn²⁺ in cell culture conditions as compared to the PCL fibrous scaffold. The combined advantages of CH and Zn in the PCL scaffold enriched 3T3 fibroblast cells' survival and proliferation except the ones with the higher concentration of Zn particles. These new composite scaffolds are promising and can be further considered for tissue healing and regeneration applications.

KEYWORDS: nanofibrous scaffold, polycaprolactone, chitosan, zinc metal, in vitro degradation, tissue engineering

1. INTRODUCTION

In recent years, polymer scaffolds modified with metal and metal compound particles such as silver, gold, iron (Fe), titanium, magnesium (Mg), and Zn have witnessed outstanding research progress in the field of biomedicine. 1-3 Several unique properties of metals such as electrical and thermal conductivity, chemical and mechanical properties, and antibacterial properties can be incorporated into composite scaffolds to enhance their applicability in the field. Mg metals are considered for structural applications such as orthopedics due to their low weight and rigidity. However, Mg degrades quickly (1-4 months) with hydrogen gas release. Fe metals have good mechanical property but degrade slowly (over 2-3 years) with degradation products stuck in tissues.⁴ Zn metal and its composite materials gained prominence due to their intrinsic physiological relevance, biodegradability, and adaptability in tissue healing and regeneration.5,6 The Zn

degradation rate is between those of Mg and Fe, and its degradation products are fully bioresorbable without hydrogen gas evolution. Zn-based implants are becoming more popular in orthopedic and vascular applications because they disintegrate at a desired rate that corresponds to the rate at which the surrounding tissues recover, hence facilitating tissue remodeling and growth.⁷ In orthopedic applications, implants coated with Zn and its compounds help in osteointegration and prevent biofilm formation.⁸ In vascular applications, pure

Received: July 6, 2023 Accepted: October 3, 2023



Zn implants regularly develop neointima around surfaces and circumvent inflammatory infiltrates for up to 11 months.^{7,9}

Zn ions, i.e., Zn²⁺, a product from the degradation of Zn, are predominantly stored in the skeletal muscle (60%) and bone (30%), with only a minute amount in the blood circulating at a concentration of $10-20 \mu M$. Just a little amount of the Zn²⁺ that exists in free labile form $(0.1-2 \mu M)$ is absorbed by blood cells, endothelial cells, and platelets. 10 Zn concentrations ranging from 7 to 20 nM increase alkaline phosphatase (ALP) activity and the mineralization of bone 11 and also improve osteogenesis by stimulating collagen production. Zn has the potential to bind with over 2000 transcriptional factors 12 and over 300 enzymes (a typical enzyme is superoxide dismutase (SOD), which functions as a free radical scavenger). ¹³ Zn²⁺ is a well-known antibacterial agent that attacks viruses, fungi, bacilli, and other bacteria and is directly involved in activating additional reactive oxygen species (ROS) generation and maintaining insulin structural integrity. 15 In the wound repair process, Zn²⁺ is very beneficial at all four stages of the repair, i.e., hemostasis, inflammation, proliferation, and tissue remodeling phases. 16

Only a few studies have established the effects of the implantation of biodegradable Zn-based metal in the body. Nevertheless, experts suggest that more priority be given to the Zn toxicity after degradation of the Zn implants. ^{17,18} The amount of Zn²⁺ released from a typical Zn-based implant over time when it is implanted in the body varies depending on several factors, such as the type of implant, the implantation period, and the degradation rate of the implant. 19 The degradation rate of bone implants is between 0.2 and 0.5 mm y⁻¹ for complete bone healing. Pure Zn does not meet the requirements of biodegradable orthopedic implants because it has a degradation rate of approximately 0.1 mm $y^{-1.20}$ Although high amounts Zn²⁺ have been shown to kill cells in their physiological environment, it is a required micronutrient in the living system like several other metal cations, e.g., Mg, Fe, and Cu, playing a direct role in cell metabolism, DNA synthesis, and proliferation, ^{21–23} Additionally, the exploration of elemental Zn in a particulate form has been a challenge because it exhibits localized and rapid degradation in an aqueous medium and tends to produce toxic levels of Zn²⁺ in a short amount of time. The release of such beneficial Zn2+ in a physiologically mimicking environment should therefore be controlled.

A possible solution to overcome the above challenges of the rapid and localized release of Zn2+ as well as several other metal micronutrients is to incorporate the metal particle into biodegradable polymer scaffolds for controlled release studies. 24-26 Unique metallic composite matrices may be created integrating biodegradable metal particles into electrospun biopolymer scaffolds to give tissue healing effects.²⁷ Biodegradable metals are expected to corrode gradually after their utilization without eliciting an adverse response to maintain mechanical integrity.^{28,29} Electrospun scaffolds are a proven suitable material for wound dressing due to their high porosity that increases the permeability for oxygen, water, and cell nutrients while protecting the wound from bacteria and dehydration.³⁰ Metal particle-containing electrospun scaffolds have been proven to improve the properties of the parent fibers without interfering with biocompatibility during the wound healing process.

Poly(ε -caprolactone) (PCL) is a synthetic semicrystalline polymer with excellent mechanical and degradation properties

that has been widely utilized in the production of metal-based scaffolds to stimulate wound healing and treat chronic wounds. PCL, however, lacks bioactivity and degrades at a much slower rate than other popular biodegradable polymers such as poly(lactic acid) and poly(lactic-co-glycolic acid). These limitations can be controlled by altering the chemical structure, molecular weight, and crystallinity of the PCL by combining it with other hydrophilic and bioactive polymers like chitosan, collagen, and gelatin, among others. 32,33

The analysis of the Zn contents in a recent study showed that the PCL/Zn scaffolds progressively stimulated osteoclastogenesis with increased Zn concentration, and the study also showed that the activation of the Wnt/ β -catenin and NF- κ B signaling pathways by Zn²⁺ resulted in osteogenesis and osteoclastogenesis regulation.³⁴ Another study showed that the PCL-nano zinc oxide (nZnO) electrospun scaffolds enhanced cell adhesion and osteogenic effects for bone tissue regeneration.³⁵ ZnO nanoparticle (NP) loaded scaffolds reduced inflammation and accelerated wound healing on a second-degree burn dressing in another study.³⁶ Although these recent efforts in fabricating Zn-based scaffolds are encouraging, much more remains to be explored and improved, particularly in the perspective of a controlled and predictable rate of release of Zn²⁺ to make the scaffolds efficient for broad applications.

In this work, we sought to fabricate PCL and PCL-chitosan (PCL-CH) scaffolds embedded with elemental Zn particles and investigate how Zn affects physical, chemical, and biological properties in vitro. Experimental methodology to incorporate elemental Zn particles into polymer scaffolds under an inert environment and analysis of the composite scaffolds will be selected based on our previously published researched work with elemental Mg.²⁶ We hypothesize that Zn embedded in PCL and PCL-CH can aid in the controlled release and degradation of Zn²⁺. PCL-Zn and PCL-CH/Zn scaffolds would have improved physicochemical properties and more beneficial biological properties that would be suitable for wound healing and other tissue engineering applications.

2. MATERIALS AND METHODS

2.1. Materials. PCL (average Mn 80,000), zinc nanoparticles (Zn NPs) (40–60 nm or 0.04–0.06 μ m), and Zn standard for ICP (1000 mg/L Zn in nitric acid) were purchased from Millipore Sigma (St. Louis, MO, USA). Chitosan oligomer (MW 7.5k) was purchased from Creative PEG Works (Chapel Hill, NC, USA). 2,2,2-Trifluoroethanol (TFE) and hexafluoro-2-propanol (HFIP) were purchased from Alfa Aesar (Ward Hill, MA, USA). Dulbecco's phosphate-buffered saline (DPBS) and Dulbecco's modified Eagle's medium (DMEM) were obtained from Life Technologies (Grand Island, NY, USA). Alamar Blue and lactate dehydrogenase (LDH) assay kits were purchased from Thermo Fisher Scientific (Waltham, MA, USA).

2.2. Preparation of PCL/Zn and PCL-CH/Zn Solutions. PCL and CH solutions were prepared at a concentration of 10% (w/w) in TFE and HFIP, respectively. PCL/Zn solutions were prepared with different concentrations of Zn particles. First, commercially available Zn NPs were added to the TFE solution under inert conditions followed by an ultrasonic bath (Ultrasonic Cleaner, PS-10A Jeken) at ice freezing temperature for 10 min for homogeneous dispersion of the particles. Dry PCL pellets were then added to the Zn solution. Five different solutions with varied concentrations of Zn (i.e., PZ-0, PZ-10, PZ-20, PZ-30, and PZ-50) were prepared with the numbers 0, 10, 20, 30, and 50 representing how much percent of Zn was mixed with the PCL polymer. Also, five different solutions (PCL-CH/Zn solutions) with varied concentrations of Zn identified as PCZ-0, PCZ-

10, PCZ-20, PCZ-30, and PCZ-50 were prepared by keeping the same weight ratio of Zn in terms of the total dry polymer weight. PCL-Zn solutions were prepared first, and CH solutions were added in such a measure so that the ratio of PCL and CH is 70:30 to reduce viscosity and prevent clogging during electrospinning. A higher chitosan ratio with PCL such as 40/60 and 50/50 from previous experiments resulted in a more viscous solution that clogged the syringe during electrospinning. An extremely low chitosan ratio such as 90/10 was unable to significantly affect the PCL as wanted. The 70/30 ratio was adopted as optimum from previous publications from our lab and others. 37,38 The mixed solutions were subjected to constant magnetic stirring for 24 h at room temperature followed by the ultrasonication to achieve homogeneity (Supporting Information, Figure S1). The sample designation and compositions of the scaffolds are given in Tables 1 and 2.

Table 1. PCL/Zn Sample Designation and Composition

scaffold name	$\begin{array}{c} \text{proportion of PCL/Zn} \\ \text{(w/w)} \end{array}$	weight of Zn in dried composite (w:w %)
PZ-0	100:0	0
PZ-10	100:10	9
PZ-20	100:20	16
PZ-30	100:30	23
PZ-50	100:50	33

Table 2. PCL-Chitosan/Zn Sample Designation and Composition

scaffold name	proportion of PCL/CH (w/w)	proportion of PCL-CH/Zn	weight of Zn in dried composite (w:w %)
PCZ-0	70:30	100:0	0
PCZ-10	70:30	100:10	9
PCZ-20	70:30	100:20	16
PCZ-30	70:30	100:30	23
PCZ-50	70:30	100:50	33

2.3. Fabrication of PCL/Zn and PCL-CH/Zn Scaffolds. The electrospinning setup and process were adopted from our earlier experiments to fabricate scaffolds. 26,37 Briefly, a syringe pump (Model 78-01001, Fisher Scientific, Pittsburgh, PA, USA), a high-voltage power supply (Model CZE100PN30, Spellman High Voltage Electronics Corporation, Hauppauge, NY, USA), and a collector drum were used to set up the experiment. Approximately 8 mL of Zn particle-loaded polymeric solution was placed in a 10 mL syringe with an attached 18 gauge-diameter hypodermic needle. The syringe tip was placed approximately 12 cm from the collector, and a 20 kV voltage supply was used to charge the solution. The flow rate was set at 2.5 mL/h. The solution was spun toward the rotating grounded drum wrapped with aluminum foil. After the electrospinning was performed, the samples were allowed to dry overnight in a chemical hood and were detached from the aluminum foil for physical, chemical, and biological characterization. The scaffolds are presented as PZ and PCZ corresponding to PCL-Zn and PCL/CH-Zn.

2.4. Dynamic Light Scattering (DLS) Analysis. The hydrodynamic size distribution of the Zn particles was measured using a Zetasizer Nano ZS (Malvern Instruments, Malvern, UK) according to our earlier publication. Prior to the measurement, 0.1 g of the asreceived industrial Zn metal powder was dispersed in 10 mL of anhydrous ethanol and sonicated for 10 min to allow good dispersion of metal particles. A 1 mL aliquot of the dispersed colloidal sample was further diluted for DLS analysis. Intensity measurements were converted into volume and number-average sizes of the particles.

2.5. Surface Morphology Analysis. The surface morphology of Zn particles, PZ, and PCZ scaffolds was analyzed using a scanning electron microscope (SEM, Zeiss Auriga series, Oberkochen, Germany) equipped with energy-dispersive X-ray spectroscopy (EDS) (Quantax 70, Bruker Corporation, Billerica, MA, USA) and

a transmission electron microscope (TEM, Zeiss Libra 120, Oberkochen, Germany). To check the morphology of Zn NPs, 0.01 g of particles was initially dispersed in 15 mL of TFE, and a single drop of solution was placed on an aluminum foil followed by evaporation of the solvent. Next, the foil piece was attached to the sample holder with double-sided carbon tape and observed under the SEM. In the case of PZ and PCZ scaffolds, samples were cut into small pieces, attached to copper tape, and sputter-coated with goldpalladium using a coating system (Leica EM ACE200, IL, USA) for 30 s (coating depth = 5 nm) at 15 mA. SEM images were taken at an accelerating voltage of 3 kV. The fiber size distribution was analyzed through SEM images with the use of the ImageJ software (NIH, Bethesda, MD, USA). The diameter length was converted to pixels with the help of a scale bar. Fifty individual fibers of PZ and PCZ samples from each group (n = 3) of SEM images were measured in pixels. The average size and standard deviation were calculated based on converted ImageJ data. EDS, a feature of SEM (Hitachi SU8000, Tokyo, Japan), was used to collect elemental data on the PZ and PCZ scaffold samples. The Aztec One software was used to semiquantitatively analyze the data. For TEM analysis, fiber samples were collected and attached directly to the carbon grid before imaging. The scaffold dimensions such as the length and width were recorded using a meter rule tracing and maintained constantly at 40 × 15 mm. The weight of the scaffolds was taken using the balance, and the thickness of the scaffold was taken using the digital micrometer screw gauge. The surface area and surface area per unit weight were estimated using the respective dimensions measured. The apparent density and porosity of each scaffold were estimated from previous publications.2

2.6. X-ray Diffraction Analysis. PCL/Zn and PCL-CH/Zn scaffold samples for XRD analysis were prepared by cutting each scaffold into a rectangular shape ($20 \times 10 \text{ mm}^2$) and attaching them to a glass slide using double-sided tape. A Bruker AXS D8 Discover X-ray diffractometer (Billerica, MA) with Cu K α radiation was used to investigate the scaffolds' diffraction patterns or crystallography and phases. The X-ray diffraction experiments were performed using a locked-coupled scan with a scanning range (diffraction angle, 2θ) set between 10 and 60° at room temperature in continuous mode and at increments of 0.0146° at room temperature.

2.7. Fourier-Transform Infrared Spectroscopy (FTIR) Analysis. To identify the functional groups and chemical interactions among the different scaffolds, FTIR was used. The Varian 670 FTIR Spectrophotometer (Varian, Inc., Palo Alto, CA, USA) was used to complete the FTIR spectra in the 4000 to 6000 cm⁻¹ region. To demonstrate the modifications that the polymer (PCL) underwent during electrospinning with Zn particles with and without the inclusion of chitosan, selected IR bands of carbonyl and ester groups, as well as CH bending, were studied.

2.8. Differential Scanning Calorimetry (DSC) and Thermogravimetric Analysis (TGA). To evaluate the temperature and heat flow associated with the different scaffold compositions as a function of time and temperature, DSC analysis was conducted on a DSC Q2000 differential scanning calorimeter (TA Instruments Co., USA) over the temperature range of 20 to 160 °C at a constant heating rate of 10 °C/min, and the first thermal transition peaks were used to establish the melting temperature $(T_{\rm m})$. The degree of crystallinity of the scaffolds will be determined by measuring the heat of enthalpy under a DSC thermogram. See details in the Supporting Information. TGA measurement was conducted on a TGA Q50 thermogravimetric analyzer (TA Instruments Co., USA) in a platinum pan with temperature controlled from (room temperature) 25 to 650 °C at a heating rate of 10 °C/min under an argon environment.

2.9. Mechanical Property Analysis. Mechanical properties of the scaffolds were determined using an Instron 5542 (Canton, MA, USA) according to our previous publication. 26,32 Briefly, a customized paper template (50×35 mm) was constructed as a sample holder to prevent sample damage from handling and to preserve uniformity in loading circumstances. A 40×15 mm scaffold sample (n = 5) was designed prior to sample testing. The sample was held at about 10 mm firmly at both ends of the customized paper template with

double-sided adhesive tape for the pneumatic jaw gripping during the experiment. The thickness of the scaffolds was measured with a digital micrometer at three locations of the scaffold, and an averaged value was used as thickness. Prior to the start of the test, the template's two halves were cut at both sides. Samples were stretched until they broke with a 500 N load cell and a set displacement rate of 3.5 mm/min. A control resolution of 0.15 $\mu \rm m$ was recommended for the type of equipment utilized. A force—displacement curve was generated after each run. The load values (recorded in N) were divided by the minimum cross-sectional area (mm²) to get stress values (MPa). Strain values were attained by dividing displacements by the initial gauge length. The stress—strain curve was generated by plotting the stress—strain values using Origin Pro. Data were further estimated for the Young's modulus (YM) and ultimate tensile strength (UTS) of the scaffolds.

2.10. In Vitro Release Study of Zn²⁺. To measure the concentration of Zn2+ ions released from the scaffolds of PZ and PCZ, 10×10 mm sample pieces were cut and attached in the wells of a 24-well plate with a surgical silicone adhesive (Kwik-Sil). The samples were sterilized by incubating in 90% ethanol for 30 min, after which samples were washed with DI water two times and placed under UV light in a sterile fume hood for about 3 h. One milliliter of the complete medium that is DMEM supplemented with 10% fetal bovine serum (FBS) and 1% antibiotics (10,000 units per mL of penicillin and 10,000 μg mL⁻¹ of streptomycin) was then added to each well and incubated in a cell culture incubator at 37 °C and 5% CO2 atmosphere. At each time interval, media were collected and replenished with new media. Free Zn²⁺ concentration was measured for each time point after the dilution with inductively coupled plasma optical emission spectroscopy (ICP-OES Optima 8300, PerkinElmer, Shelton, Connecticut).

The collected solution was pretreated before measurement. Briefly, the samples were pipetted precisely, with a volume of 1 mL, into digestion tubes, and concentrated nitric acid (67–70%, Fisher Scientific) and hydrofluoric acid (48–51%, VWR Chemicals) were added to each tube. A predigestion process of 10 min was allowed before transferring the digestion tubes to an automated sequential microwave digester (MARS 6, CEM Microwave Technology Ltd., North Carolina, USA). The resulting product was a clear and transparent aqueous solution, which was further diluted to 50 mL by using double DI water. To establish a calibration curve, a set of matrix-matched standards was prepared. All of the samples were then analyzed using the Optima 8300 ICP-OES instrument. The detailed parameters for microwave-assisted acid digestion of samples are shown in Supporting Information Tables S3 and S4.

2.11. Cell Culture Study on Fibrous Scaffolds. *2.12.1. Cell Preparation.* NIH-3T3 mouse fibroblast cell lines (American Type Culture Collection, ATCC Cell Line Bank 1658, Manassas, VA, USA) were cultured with the complete medium at 37 °C with 5% CO₂ and 95% humidified atmosphere. The medium was replaced every second day of culture. Upon confluency, cells were passaged by trypsinization before seeding.

2.12.2. Cell Seeding to PZ and PCZ Scaffolds. The different scaffolds (n=4 per sample) with dimensions of 12×12 mm² were fixed into the 48-well plates and sterilized under UV overnight. The samples were then washed with 70% ethanol followed by washing with phosphate-buffered saline (PBS, Gibco; Life technologies). The samples were again pretreated overnight with the complete media. Cells at a density of 5×10^4 were seeded on each scaffold by pipetting onto the center and cultured in the incubator for 1 to 3 days. The cells were nourished with fresh medium every second day. However, for cell viability and toxicity studies, medium extracts were collected each day and stored.

The cytocompatibility of the PZ and PCZ scaffolds was also examined using an indirect method as adopted from Brown et al. and other publications. ^{40,41} Briefly, the PZ and PCZ scaffolds were immersed in the complete medium for 14 days. Scaffold extracts were collected and then seeded with 3T3 fibroblast cells that were preprepared as described in Section 2.12.1. At each time period (e.g.,

1, 2, and 3 days), media from cell-laden scaffolds were collected and stored for cytotoxicity evaluation.

2.12.3. Cell Viability and Toxicity Analysis. The cell viability of 3T3 cells was examined using the Alamar Blue (AB) colorimetric assay as described in a previous work.⁴² Briefly, the cell-laden fibrous scaffolds were treated with 10% AB reagent in cultured media and incubated for 4 h. Assay solutions were transferred to 96-well plates to measure fluorescence (530 nm excitation and 590 nm emission). The cell toxicity of PZ and PCZ scaffolds was evaluated using a Pierce LDH assay kit following the manufacturer's instruction and also with reference to our previous work. 43,44 Briefly, 50 μ L of collected sample media (n = 3) was transferred to a 96-well plate and mixed with a 50 μL reaction mixture. The plate was covered with aluminum foil and incubated at room temperature for 30 min. Fifty microliters of stop solution was added to each well to stop the reaction, and the absorbance of the samples was measured at 490 and 680 nm by a microplate reader (CLARIOstar Plus, BMG LABTECH Inc., Cary, NC, USA).

The adhesion, proliferation, and survivability of the cells on the scaffolds were examined with a live/dead assay kit (PerkinElmer LLC Via AOPI Staining Solution; Fisher Scientific, USA) in accordance with the company's protocol. The live and dead cells stained in green and red color, respectively, were visualized and captured with an Olympus IX83 microscope incorporated with the Olympus cellSens Dimension software (Olympus Corporation, Shinjuku, Tokyo, Japan). Live and dead cells were counted from the fluorescence images using ImageJ 1.53c (NIH, Bethesda, MD, USA).

In addition, the morphology of the viable cells was visualized under a fluorescence microscope in the cells cultured for 1 to 3 days. For that, the cells were seeded at a density of 1.5×10^4 cells/well. After a predetermined period, the cells were washed twice with PBS before fixing with 4% paraformaldehyde (PFA, Thermo Fisher Scientific) solution for 10 min and permeabilized in 0.2% Triton (X-100) (Thermo Fisher Scientific) for 2 min at room temperature. The cells were blocked with 1% bovine serum albumin (BSA) for 30 min after washing with PBS. The cells attached on the scaffolds were consequently stained by Actin Green 488 Readyprobes reagent (Invitrogen, Thermo Fisher Scientific) for the cytoplasm (20 min) and DAPI (4'6-diamidino-2-phenylindole dihydrochloride; Invitrogen, Thermo Fisher Scientific) for nuclei (5 min) at room temperature in the dark condition. After washing three times with PBS, fluorescence images were taken using an Olympus IX83 microscope (Olympus).

2.12.4. Cell-Fibrous Scaffold Preparation for SEM Imaging. Furthermore, the cellular mass attachment, proliferation, and morphology were analyzed using SEM following the procedure from our previous publication. ²⁶ Briefly, the attached cells were rinsed twice with PBS and fixed with 4% glutaraldehyde for 30 min. After fixation, cells were rinsed with deionized water (2 times) and dehydrated with successive incubations in 50, 75, and 100% ethanol, leaving 10 min each time, at room temperature. The cell samples were left to dry in a sterile fume hood for 24 h and then cut to fit on the ring and sputter coated for about 3 min before images were taken.

2.12. Statistical Analysis. All data were presented as mean \pm standard deviation (S.D.) and were analyzed using one-way analysis of variance (ANOVA) for significance with the OriginPro software version 2023 (Origin Lab, Northampton, MA, USA). Post hoc Tukey's test and Holm–Sidak test were performed with ANOVA for multiple comparisons. The α value was set to 0.05, 0.01, and 0.001, and p values less than 0.05 and 0.001 were considered statistically significant.

3. RESULTS

3.1. Characterization of Zn Particle and Electrospun Scaffolds. *3.1.1. Size and Morphology of Zn NPs.* Before the Zn particles were dissolved in the solvent with PCL or PCL-CH as shown in Figure S1, the size, morphology, and crystalline properties of the as-received commercial Zn particles were investigated before they were incorporated.

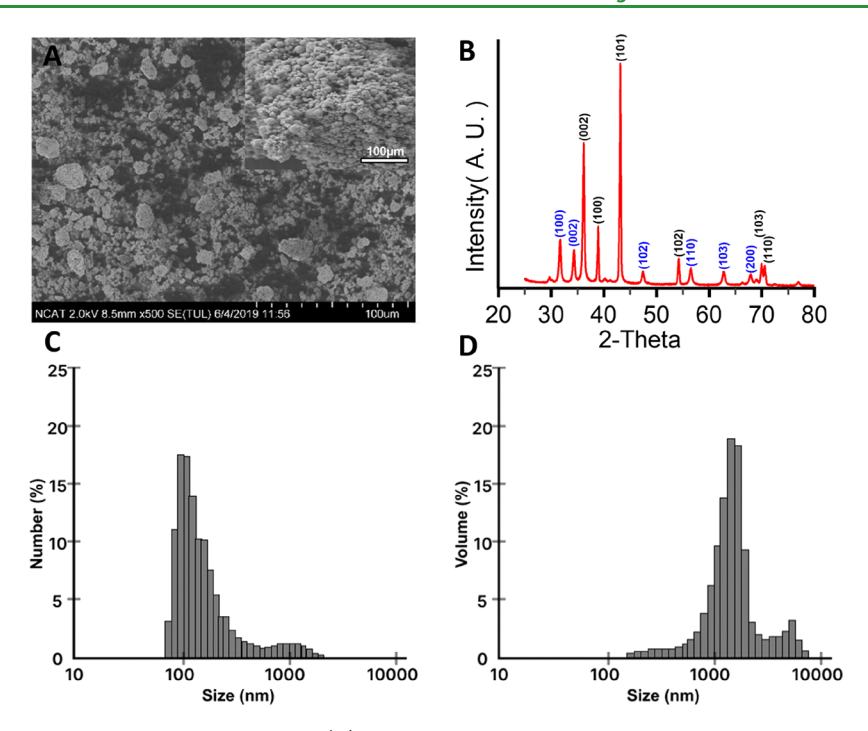


Figure 1. Characterization of as-received Zn metal particles. (A) SEM images of Zn particles at low magnification with inset at high magnification (scale bar = $100 \ \mu m$). (B) X-ray diffraction pattern revealing crystallographic planes of Zn. The size distribution of as-received Zn particles was measured using the DLS technique. (C, D) The average hydrodynamic diameter of the particles measured from number and volume-weighted distributions obtained from DLS, respectively.

The SEM image in Figure 1A and TEM image in Figure S2 C reveal the morphology of the pure Zn powder. The metallic particles were obtained as mixed powder of aggregated particles and ultrasmall and large particles in the size range of 70 to 10,000 nm. Figure 1B shows the X-ray diffraction results for the particles, and the peaks correspond to the known crystallographic planes of Zn. The XRD patterns of the Zn particles show characteristic peaks at 36.34, 39.06, 43.28, 54.36, 70.1, and 70.68° corresponding to diffraction planes of metallic Zn at (002), (100), (101), (102), (103), and (110), respectively. In addition, new peaks were observed at 31.8355, 34.5207, 47.5808, 56.6487, and 62.8917° corresponding to (100), (002), (102), (110), and (103) planes of ZnO, respectively, suggesting that the Zn slightly oxidized.

Most of the particles had a mean hydrodynamic diameter of about 100 nm (Figure 1C), and the volume percentage was distributed between 1000 and 10,000 nm.

3.1.2. Morphology of PCL/Zn and PCL-CH/Zn Scaffolds. The fibrous morphology and diameter distribution of asprepared PZ and PCZ scaffolds are shown in Figure 2. Fiber morphology varied drastically with the change in particle concentration. Compared to PCL, many beads can be observed on both PZ and PCZ fibers, indicating the presence of Zn particles. Notably, particles aggregated on the surface of the fiber as the concentration of Zn increased. Smooth and relatively uniform fibers were generally obtained with smaller fractions of the particles. In contrast, a distinct surface roughness or rugged surface was observed with the high concentration of NPs within and on the fibers. The NPs of smaller diameters were encapsulated within the fibers, whereas the relatively larger ones were on the fiber. The diameters of PZ fibers as shown in Figure 2A-E were measured and found to range between 0.3 and 2.4 μ m with the average diameter of PZ-0, PZ-10, PZ-20, PZ-30, and PZ-50 estimated as 1.31 \pm

0.5, 0.81 \pm 0.3, 1.07 \pm 0.5, 0.97 \pm 0.4, and 1.02 \pm 0.5 μ m, respectively, confirming that the Zn particle integrated fibers showed smaller diameters than pure PCL fibers.

The SEM images of Figure 2F–J also confirm that chitosan integrated PCZ scaffolds are also homogeneous and have a bead-free fiber morphology. The fibers are regular and continuous at a lower ratio of Zn, but the presence of a higher percentage of Zn particles modified the surface morphology of the fibers significantly. Agglomeration of the Zn particles can be clearly observed in the images of PCZ scaffolds with a higher percentage of Zn particles. The average diameters of chitosan integrated scaffolds were measured and found to be 1.34 ± 0.3 , 0.69 ± 0.2 , 0.57 ± 0.1 , 0.53 ± 0.2 , and $0.41 \pm 0.1~\mu m$ for PCZ-0, PCZ-10, PCZ-20, PCZ-30, and PCZ-50, respectively. Overall, the diameters of the PCZ fibers are smaller than those of the PZ fibers without chitosan.

The distribution of Zn within the scaffold was confirmed by SEM-EDS analysis, which also showed the elemental mapping of Zn particles obtained from the SEM image (Figure S2A,B). Transmission electron microscopy images further confirmed Zn particles in their aggregated form and encapsulated within the individual fiber (Figure S2 C). The surface area, apparent density, surface area per unit weight, and porosity of the scaffolds were estimated using a fixed rectangular dimension of the PZ and PCZ scaffold samples (i.e., 40×15 mm) and other prior measurement such as the weight of the sample (see results in Supporting Information, Tables S1 and S2). The thicknesses of the PZ-0, PZ-10, PZ-20, PZ-30, and PZ-50 scaffolds were estimated in millimeters (mm) as $0.148 \pm$ 0.0034, 0.156 ± 0.0041 , 0.169 ± 0.0052 , 0.184 ± 0.0043 , and 0.211 ± 0.0033 , respectively. The thicknesses of the PCZ-0, PCZ-10, PCZ-20, PCZ-30, and PCZ-50 were estimated also in mm as 0.140 ± 0.0016 , 0.149 ± 0.0041 , 0.153 ± 0.0027 , 0.175 \pm 0.0028, and 0.201 \pm 0.0031, respectively. All the Zn-

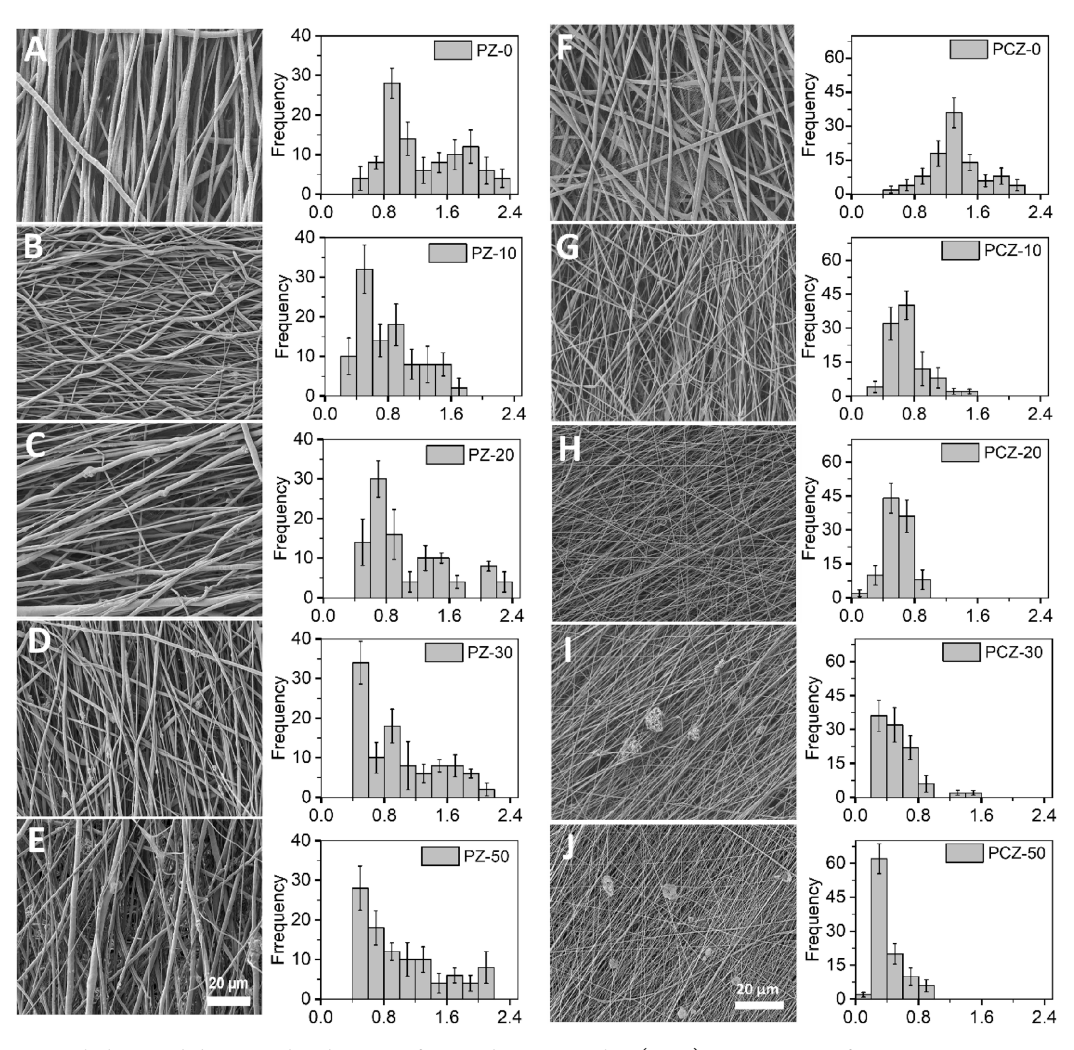


Figure 2. Surface morphology and diameter distributions of PZ and PCZ samples. (A–E) SEM images of PZ-0 to PZ-50, respectively, and their corresponding histogram showing the distribution of fiber diameters of the as-prepared PZ-0 to PZ-50 samples. (F–J) SEM images of PCZ-0 to PCZ-50, respectively, and their corresponding histogram showing the distribution of fiber diameters of the as-prepared PCZ-0 to PCZ-50 samples.

containing scaffolds had slightly increased thickness compared with the pure PCL scaffolds. The surface areas per unit weight of each fibrous scaffold sample expressed in m²/g were 3.4 \pm 0.61, 3.1 \pm 0.09, 2.9 \pm 0.62, 2.8 \pm 0.32, and 1.4 \pm 0.41 for PZ-0, PZ-10, PZ-20, PZ-30, and PZ-50, respectively, and those of the PCZ fibers were estimated as 2.5 \pm 0.38, 1.8 \pm 0.21, 1.5 \pm 0.27, 1.4 \pm 0.44, and 1.1 \pm 0.62 for PCZ-0, PCZ-10, PCZ-20, PCZ-30, and PCZ-50 in that order.

It was also found that the concentration of particles in fibers affected the thickness of the sample, which reveals why the increase in particle concentration increased the thickness of the scaffolds. The average porosity percentage of PZ-0 and PZ-50 ranged between 51 \pm 5.7 and 60 \pm 5.6, and that of PCZ-0 and PCZ-50 was between 62 \pm 5.3 and 76 \pm 6.1, respectively. These values were obtained using eqs 1–3 in the Supporting Information. All of the results suggested that the presence of the particles increased the surface area per unit weight and porosity of the scaffolds. As noted with the porosity numbers, the lower fiber diameters for PCZ were attributed to the higher porosities in higher Zn samples.

The impact of both Zn and CH on the hydrophilicity of PZ and PCZ scaffolds was also investigated using contact angle measurement. The details of measurements and outcome of our investigation are given in the Supporting Information

document (Table S3). The average contact angles for PZ-0, PZ-10, PZ-20, PZ-30, and PZ-50 were 127 ± 4.3 , 97 ± 1.1 , 71 ± 2.6 , 70 ± 3.3 , and 74 ± 7.2 , respectively. The average contact angles for the PCZ scaffolds were 59 ± 1.2 , 59 ± 3.5 , 54 ± 4.2 , and 52 ± 5.6 for PZ-10, PZ-20, PZ-30, and PZ-50, which make the PCZ samples have high surface energy. There was no contact angle measurement for the PCZ-0 samples because there was difficulty capturing the images after the drop because it drained so fast in the fiber.

3.1.3. FTIR and XRD Analysis of Electrospun Scaffolds. FTIR spectra were measured to confirm any chemical changes in the chemical composition of PCL and CH while incorporating the Zn NPs (Figure 3A,B). The characteristic absorption peak of PCL was located at 1727 cm⁻¹ for the stretch of CO in ester groups and 1240 and 1170 cm⁻¹ for asymmetric and symmetric stretching vibrations of C-O-C. These characteristic peaks in the PCL are consistent with the previously reported results and showed no new or significant changes in peak position in PCL after encapsulation of Zn NPs. This suggests that the addition of the Zn particles did not significantly alter the chemical structure of the PCL. Additional peaks in PCZ fibrous scaffolds were observed at 1533 and 1662 cm⁻¹ corresponding to amine and amide groups of chitosan. These results confirm the presence of CH in all PCZ.

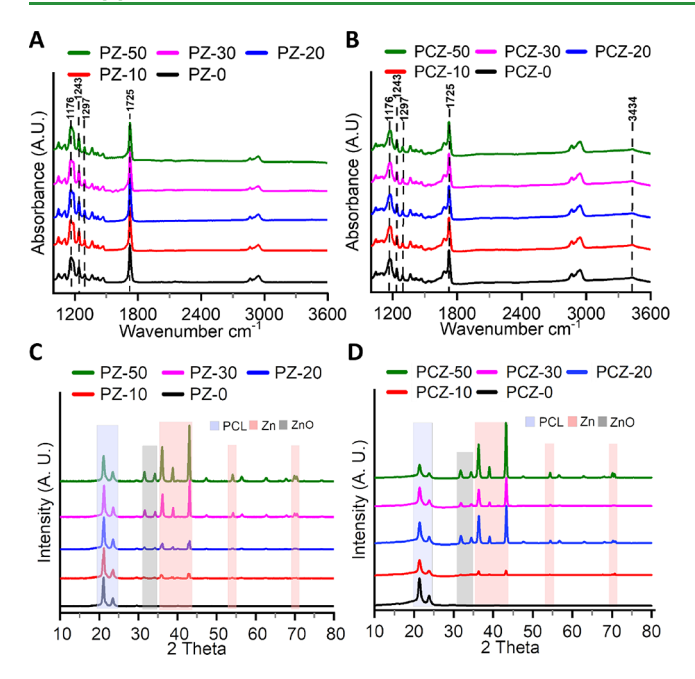


Figure 3. Analysis of crystalline phases and chemical structure of the scaffolds with different concentrations of Zn NPs. (A, B) ATR-FTIR spectra of the PZ and PCZ samples, respectively. (C, D) XRD patterns of PZ and PCZ samples, respectively.

To analyze possible changes in the crystallinity of the PZ and PCZ scaffolds after adding Zn particles, XRD patterns were evaluated (Figure 3C,D). Characteristic peaks of PCL were observed at 21.5 and 23.6° referring to the crystallographic planes of (110) and (200), respectively.⁴⁸ The scaffolds exhibited low-intensity peaks at the same positions that are assigned to Zn NPs, suggesting the presence of Zn NPs in the scaffolds. These peak positions are similar to the Zn particles published in a previous research.⁴⁷ The intensity of the PCL peaks decreased for both PZ and PCZ scaffolds with increased Zn amounts, revealing a decrease in the degree of crystallinity of PCL. The intensity of the Zn peaks increased as the concentrations increased in both PZ and PCZ groups. The appearance of the same crystallographic peaks of Zn in all fiber samples as illustrated in Figure 1B above and the lack of any significant new peaks of Zn products strongly suggest that our method of incorporating of Zn metal particles in the scaffolds did not alter any crystalline properties of the Zn. PCZ scaffolds did not exhibit any characteristic peaks of CH, indicating that the effect of CH in the change in crystallinity of the scaffolds was not very significant.

3.1.4. DSC and TGA Analysis. Thermal behaviors of the PZ and PCZ scaffolds were analyzed by the DSC and TGA methods. The melting and crystalline temperatures of each sample are shown in Figure 4. In line with PCL's typical melting point (Tm), the scaffold samples displayed a melting endotherm at a temperature of 60 °C. All samples regardless of the group (i.e., PZ or PCZ) showed a melting endotherm ranging between 60 and about 63 °C. The percentages of crystallinity of the PZ-0, PZ-10, PZ-20, PZ-30, and PZ-50 samples were 62.0, 54.1, 53.5, 47.9, and 43.8, respectively. Those for PCZ-0, PCZ-10, PCZ-20, PCZ-30, and PCZ-50 were 57.9, 53.7, 52.7, 46.5, and 39.1 as shown in the Supporting Information (Figure S3).

The TGA curves as shown in Figure 4C,D illustrate the weight loss of the scaffolds at various onset temperatures. The

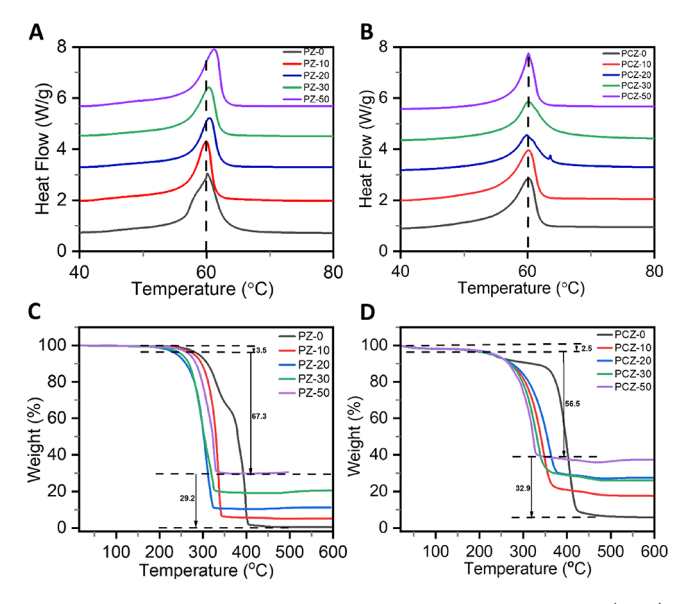


Figure 4. Thermal property analysis of PZ and PCZ scaffolds. (A, B) Representative DSC curves showing crystalline properties of the PZ and PCZ nanofiber scaffold, respectively. (C, D) TGA analysis showing the thermal stability of PZ and PCZ samples at different temperatures, respectively.

weight change curves in the TGA indicate that the control scaffolds (i.e., PZ-0) all burned out without traces of the material left, but the same trend was not observed with the Zncontaining scaffolds. The presence of the metal did not allow for the complete burning of the scaffold. The PZ-0 scaffold completely decomposed at the onset temperature close to 500 °C. However, 70% of the PZ-50 was decomposed at around that same temperature range, which can be explained by the fact that the 70% that burned was the PCL polymer and the remaining weight of about 30% representing the Zn particles was present in the fibers. Further observation of the PZ plot showed that at about 330 °C, the weight of PZ-10, PZ-20, and PZ-30 remained approximately ~9, ~12, and ~20%. The weight loss of the scaffolds was found to be lowered after the integration of CH and increased concentration of Zn NPs. Unlike PZ-50, the PCZ-50 samples had only about 60% burnout, and the remaining weight of about 40% representing the Zn particles was present in the scaffold samples. It can generally be concluded from the graph that the introduction of chitosan impacted the slow or delayed burning rate of the scaffold.

3.1.5. Mechanical Properties of Scaffolds. The mechanical properties of the scaffolds expressed in stress-strain curves, Young's modulus (YM), and ultimate tensile strength (UTS) are shown in Figure 5. The quantitative data are summarized in Tables 3 and 4. Pure PCL scaffolds showed the highest strain as compared to Zn particle containing composite scaffolds. Zn particles remarkably lowered the strain of each scaffold, suggesting that the increase in Zn NP concentration reduced the strain of the electrospun scaffolds. As expected, the tensile stress of the composite scaffold increased after particle integration. However, the stress of PZ scaffolds gradually decreased with an increment in the concentration of particles in the fibers. The presence of CH lowered both strain and stress as compared to those of PZ scaffolds. The YM and UTS of both composite scaffolds were decreased with an increased concentration of NPs.

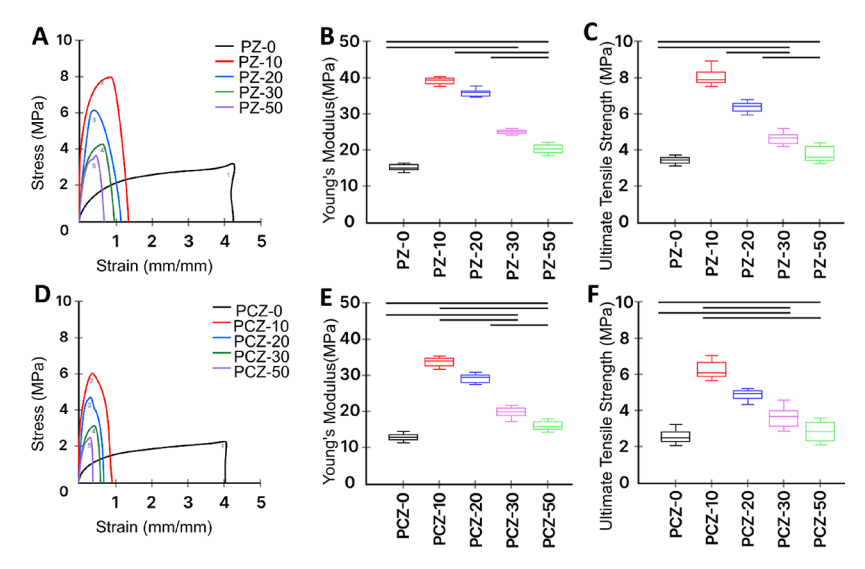


Figure 5. Mechanical properties of PZ and PCZ scaffolds investigated by tensile testing. (A, D) Representative sets of typical tensile stress—strain curves of PZ and PCZ, respectively. (B, E) Ultimate tensile strength at break for PZ and PCZ samples, respectively. (C, F) Comparisons of Young's modulus of PZ and PCZ, respectively. Bars indicate significant differences (ANOVA, p < 0.05 for each n = 5).

Table 3. Mechanical Properties of PZ Fibrous Scaffolds

fibrous scaffold	Young's modulus (MPa)	ultimate tensile strength (MPa)	breaking strain (mm/mm)
PZ-0	16.15 ± 1.9	3.51 ± 0.4	4.21 ± 0.1
PZ-10	38.29 ± 2.8	8.21 ± 0.5	1.42 ± 0.1
PZ-20	35.41 ± 3.4	6.28 ± 0.3	1.15 ± 0.04
PZ-30	25.91 ± 2.5	4.46 ± 0.2	0.94 ± 0.03
PZ-50	19.15 ± 2.7	3.84 ± 0.4	0.65 ± 0.2

Table 4. Mechanical Properties of PCZ Fibrous Scaffolds

fibrous scaffold	Young's modulus (MPa)	ultimate tensile strength (MPa)	breaking strain (mm/mm)
PCZ-0	13.71 ± 1.6	2.54 ± 0.3	4.03 ± 0.1
PCZ-10	34.73 ± 3.2	6.36 ± 0.6	0.91 ± 0.1
PCZ-20	29.58 ± 2.4	4.90 ± 0.3	0.75 ± 0.04
PCZ-30	21.14 ± 2.2	3.73 ± 0.2	0.61 ± 0.03
PCZ-50	16.95 ± 2.7	2.64 ± 0.4	0.47 ± 0.02

3.2. In Vitro Release of Zn Ions. The Zn release profiles of all PZ and PCZ scaffolds for a 14 day (336 h) degradation period are presented in Figure 6 and Figure S4. The detailed parameters for the microwave-assisted acid digestion of samples are shown in Tables S4 and S5.

The Zn release study was conducted in a culture medium at standard cell culture conditions for mammalian cells. The cumulative free release of the $\mathrm{Zn^{2+}}$ of the PZ and PCZ nanofiber scaffolds was estimated using ICP-OES quantitative analysis.

The presence of Zn^{2+} in the cumulative release profile as shown in Figure 6A,B shows a release increase in both groups (PZ and PCZ scaffolds) as the concentration of Zn particles increased in the scaffold. At the end of the experiment (336 h), cumulative releases of Zn^{2+} estimated for the PZ-0 to PZ-50 scaffolds were 0.004 \pm 0.001, 0.139 \pm 0.014, 0.172 \pm 0.009, 0.183 \pm 0.015, and 0.199 \pm 0.013 mmol, respectively. At the same time point, cumulative releases of Zn^{2+} estimated for the PCZ scaffolds were 0.011 \pm 0.001, 0.173 \pm 0.018, 0.204 \pm 0.018, 0.225 \pm 0.023, and 0.264 \pm 0.021 mmol corresponding to the samples PCZ-0 to PCZ-50, respectively.

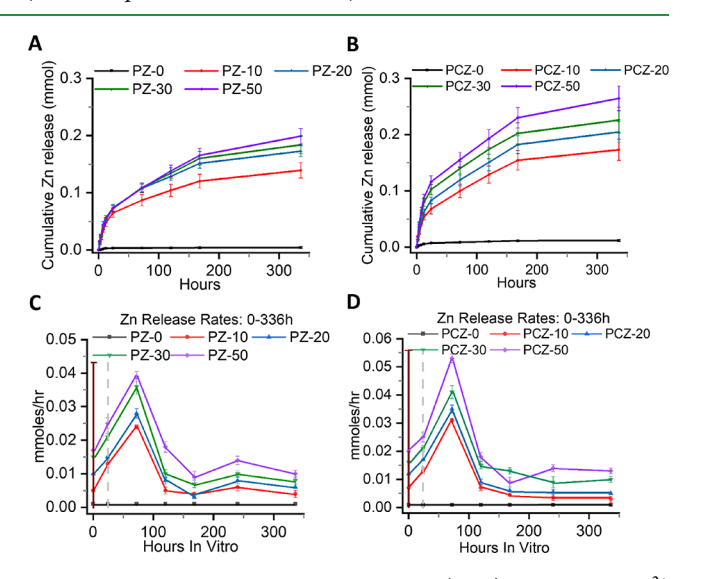


Figure 6. In vitro release study of Zn ions. (A, B) Cumulative Zn^{2+} release from scaffolds PZs and PCZs, respectively. Data are representative of multiple experiments (n=3). (C, D) Rates of Zn^{2+} release from scaffolds immersed in the culture medium from start to end points for PZ and PCZ. The amount of free Zn^{2+} released was divided by the hours of exposure to give the rates of release for each period between the media replacements.

The release profile in Figure 6A shows that the PZ group exhibited an initial burst effect at 24 h and plateaued after. However, the PCZ profile (Figure 6B) exhibited its initial burst at an earlier time point than 24 h. The cumulative release of $\rm Zn^{2+}$ from the scaffolds of PZ-20, PZ-30, and PZ-50 after 72 h did not show any significant differences (p < 0.05). However, for the PCZ groups, all the scaffolds released different amounts of $\rm Zn^{2+}$ after the same time point (72 h), which were statistically significant (p < 0.05). Also, the cumulative graph for both the PZ and PCZ groups of scaffolds indicated that the PZ-50 and PCZ-50 released more $\rm Zn^{2+}$ as expected.

The rates of free Zn^{2+} release per period were determined between medium replacements by dividing amounts of free Zn^{2+} released by hours of exposure of scaffolds immersed in the culture medium. The rate of release graph in Figure 6C,D indicates an increase in release for all samples from day 1 (i.e., 24 h) to day 3 (i.e., 72 h). The rates of release over the first 2 and 72 h were much higher than subsequent days. All samples, especially PZ-10 and PCZ-10, showed a slower release by the end of 14 (i.e., 336 h) days. Samples with the highest Zn particles, i.e., PZ-50 and PCZ-50, released more Zn²⁺ than the others. There was a gradual decrease in the amount of release after day 3 for both sample groups. However, samples never stopped releasing even after the end of the experiment time frame. The standard deviations derived by summing variances each time point were used to conduct an ANOVA on the cumulative release after 336 h for all samples. Results from all scaffold types and two different batches are shown in Supporting Information (Figure S4 A for PZ samples and Figure S4 B for PCZ sample scaffolds). There was no batch difference represented between batches of the same scaffolds (p < 0.001, n = 4). However, there were significant differences between some of the PZ (20 to 50) and PCZ (20 to 50) samples (Supporting Information Figure S4 C).

The highest amount of Zn^{2+} released was obtained from the groups containing the highest amount of Zn particles, i.e., PZ-50 and PCZ-50. The amounts of Zn^{2+} released from PZ-50 and PCZ-50 were 163.4 \pm 2.83 and 152.34 \pm 2.83 mmol/L, respectively, which are close to the reported cytotoxic levels in the ZnO-based wound dressings⁴⁹

3.3. In Vitro Cytotoxicity. Cell viability and cytotoxicity studies of the as-prepared electrospun scaffolds were assessed in vitro with fibroblasts (3T3 cells) using Alamar Blue assay and LDH assays. Cells were examined by plating the cells directly onto scaffolds, with time periods of 1, 2, and 3 days. The scaffold samples without Zn (i.e., PZ-0 and PCZ-0) were selected as our positive control. As seen in Figure 7A,C, cell

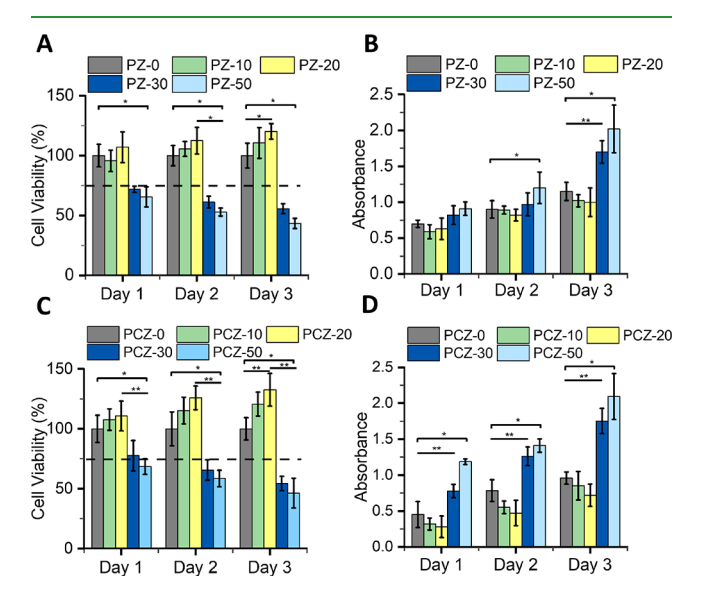


Figure 7. Fibrous scaffold performance in vitro and effects on viability and toxicity of 3T3 cells using direct test method. (A, B) Viability (Alamar Blue assay) and toxicity (LDH absorbance assay) of the cultured cells on PZ samples, respectively. (C, D) Viability (Alamar Blue assay) and toxicity (LDH absorbance assay) of the cultured cells on PCZ samples, respectively. Statistically significant values were determined using the one-way ANOVA post hoc Tukey method, and the data are expressed as the mean \pm S.D., with n=4 (where *p<0.05 and ** p<0.01).

viability data reveal that scaffolds with a lower concentration of Zn (i.e., PZ-10 and PZ-20) showed more than 100% viability by the end of day 3. In contrast, the scaffolds with a higher concentration of Zn (i.e., PZ-30 and PZ-50) showed a decrease of viability at the same period of culture time. Although the cell viability slightly improved when cultured on PCZ scaffolds, the overall viability was at the same trend as that seen with PZ scaffolds. The optical density (OD) recorded for the LDH assay (Figure 7B,D) also demonstrated that the scaffolds with a lower concentration of Zn (i.e., PZ-10 and PZ-20) exhibited no cellular toxicity, whereas the scaffolds with a higher concentration of Zn (i.e., PZ-30 and PZ-50) showed an increased trend of toxicity. Per the current ISO standards (ISO-10993-5), cell viability higher than 75% is considered to indicate no toxicity in evaluation of medical devices. 50 Our results indicate that PZ-30 and PZ-50 scaffolds might not be suitable for further studies. Nevertheless, the concentration of Zn²⁺ released from PCZ scaffolds up to day 3 was different compared with the release profile of PZ scaffolds. However, additional studies are needed to investigate the close relationship between Zn²⁺ degradation and cell responses.

The indirect cell-fibrous scaffold testing had interesting outcomes. From the graph, the PCZ created an atmosphere for an easy release of the Zn²⁺ in the media; thus, the concentration of the Zn²⁺ with the cells was direct without the fiber, which exposed the cells to toxicity anytime. However, the viability reading shows a drastic reduction in viability of the PZ compared to PCZ. Some PCZ scaffolds such as PZ-10 and PZ-20 regardless are viable to be considered for future works. The cell viability and toxicity plot for the indirect method is shown in the Supporting Information (Figure S5).

Figures 8 and 9 illustrate the cell attachment, survivability, and spreading of NIH/3T3 cells with different PZ and PCZ scaffolds at different time periods. The live/dead fluorescence image indicates that the samples with Zn²+ concentration up to 20% (PZ-20 and PCZ-20) have excellent biocompatibility and cytocompatibility to the NIH 3T3 cell line. The green and red fluorescence images showed live and dead cells, respectively. On PZ-30 and PZ-50 samples, more dead cells (red color staining) were observed, and their number continuously increased on both days 1 and 3.

The histogram plots on the right-hand side also indicate that the cell viability was excellent for the samples (PZ-10 and PZ-20; PCZ-10 and PCZ-20). More than 90% of the cells were seen to be viable. However, as the $\rm Zn^{2+}$ concentration increased (PZ-30 and PZ-50; PCZ-30 and PCZ-50) the viability % decreased. The overall result indicates that the PZ and PCZ showed excellent bioactivity to promote NIH/3T3 cell adhesion and proliferation up to a certain concentration of Zn and showed the inhibiting effect at higher concentrations, revealing a dose-dependent effect of $\rm Zn^{2+}$ concentration for cell growth. The quantitative data reveal that the scaffolds with higher % of Zn particles showed cytotoxicity. However, chitosan integrated scaffolds exhibited improved cytocompatibility.

The fluorescence images in Figure 10 show the cellular attachment, migration, and distribution of NIH/3T3 cells on the scaffolds. Basically, PZ-20 and PCZ-20 stimulate cells for proliferation and attachments. After 3 days of cultivation, a dense cellular mass with highly elongated and interconnected morphology of the cells was observed. The relatively elongated spindle shape resembles the morphology of NIH/3T3 cells in vitro under physiological conditions. The cell proliferation on

ı

ACS Applied Materials & Interfaces

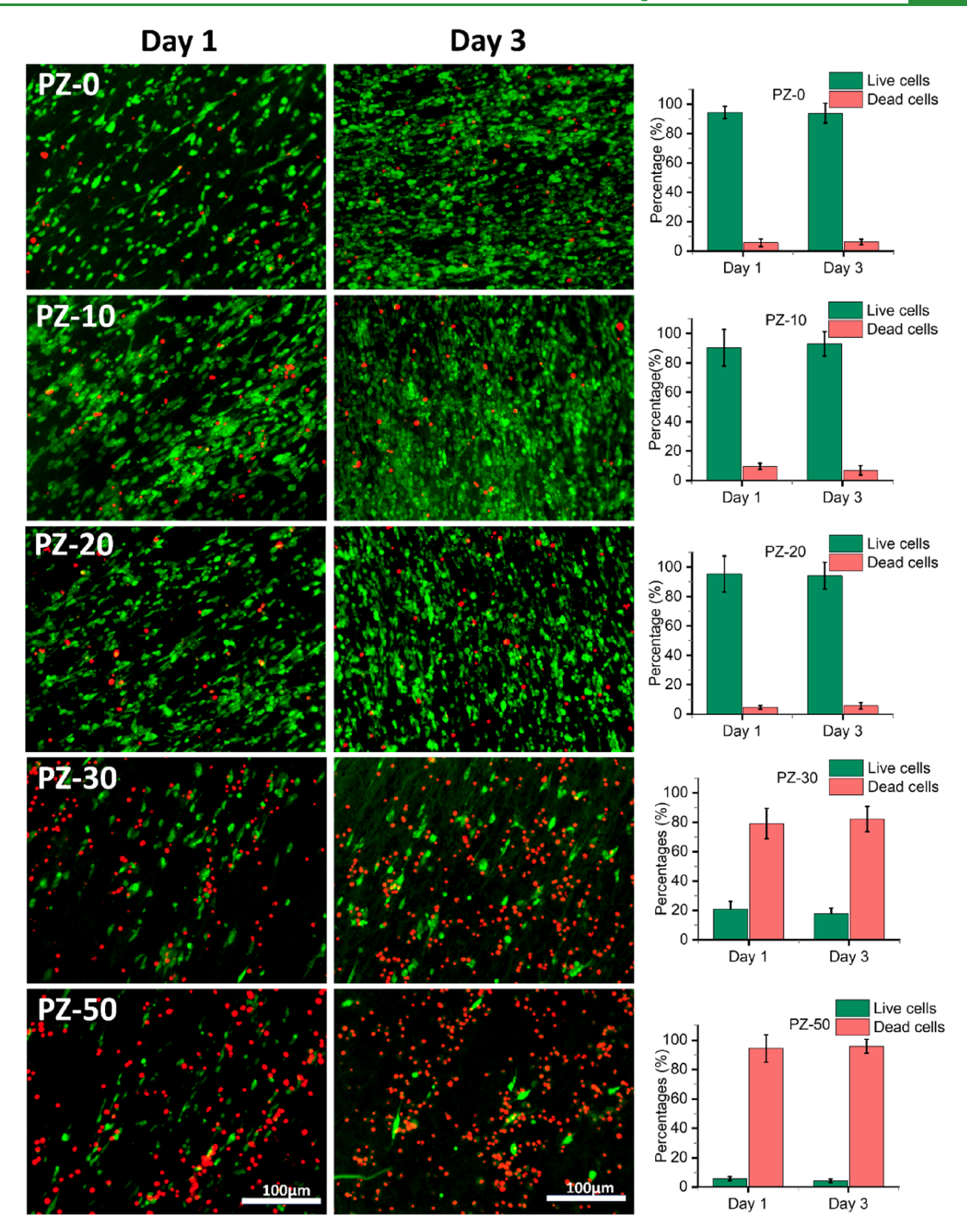


Figure 8. In vitro performance of the fibrous scaffold and effects on cell attachment and morphology. Fluorescence microscopy images represent live (stained green) and dead (stained red) NIH/3T3 fibroblasts cultured on the PZ scaffolds for day 1 (left) and day 3 (middle) utilizing acridine orange/propidium iodide (AOPI) dye (scale bar = 100 μ m). Right: Histograms show the counted percentage of live and dead cells in the corresponding fluorescence images using the ImageJ software (n = 5) of PZ-0 to PZ-50, respectively.

the scaffold with over 20% Zn particles showed an inhibitory effect for cells, indicating that the beneficial effect of Zn²⁺ is at a lower concentrations range. These results suggested that the PCZ-20 exhibited synergetic effects in cell proliferation and cell growth. The healthy growth of cells represents that the scaffolds have strong bioactivity, providing a suitable microenvironment for cell function, e.g., cell adhesion, spreading, and cell-to-cell interaction and communication. Cell—substrate adhesion and cell spreading are tightly related to cell proliferation and often accompanied by changes in structure

and cell morphology. In PZ-50 image samples, the morphology of the cells turned from spindle to round because it is at the verge of losing its growth and development and likely to experience apoptosis. Very few cells were barely observed with both PZ-50 and PCZ-50 samples. Samples of PZ-50 and PCZ-50 are shown in the Supporting Information (Figure S6). Additionally, cell organization and attachments on PZ and PCZ scaffolds were very different in comparison with the 2D flat surface as seen in the tissue culture plate (TCP) (Supporting Information, Figure S7). The cellular morphology

ACS Applied Materials & Interfaces

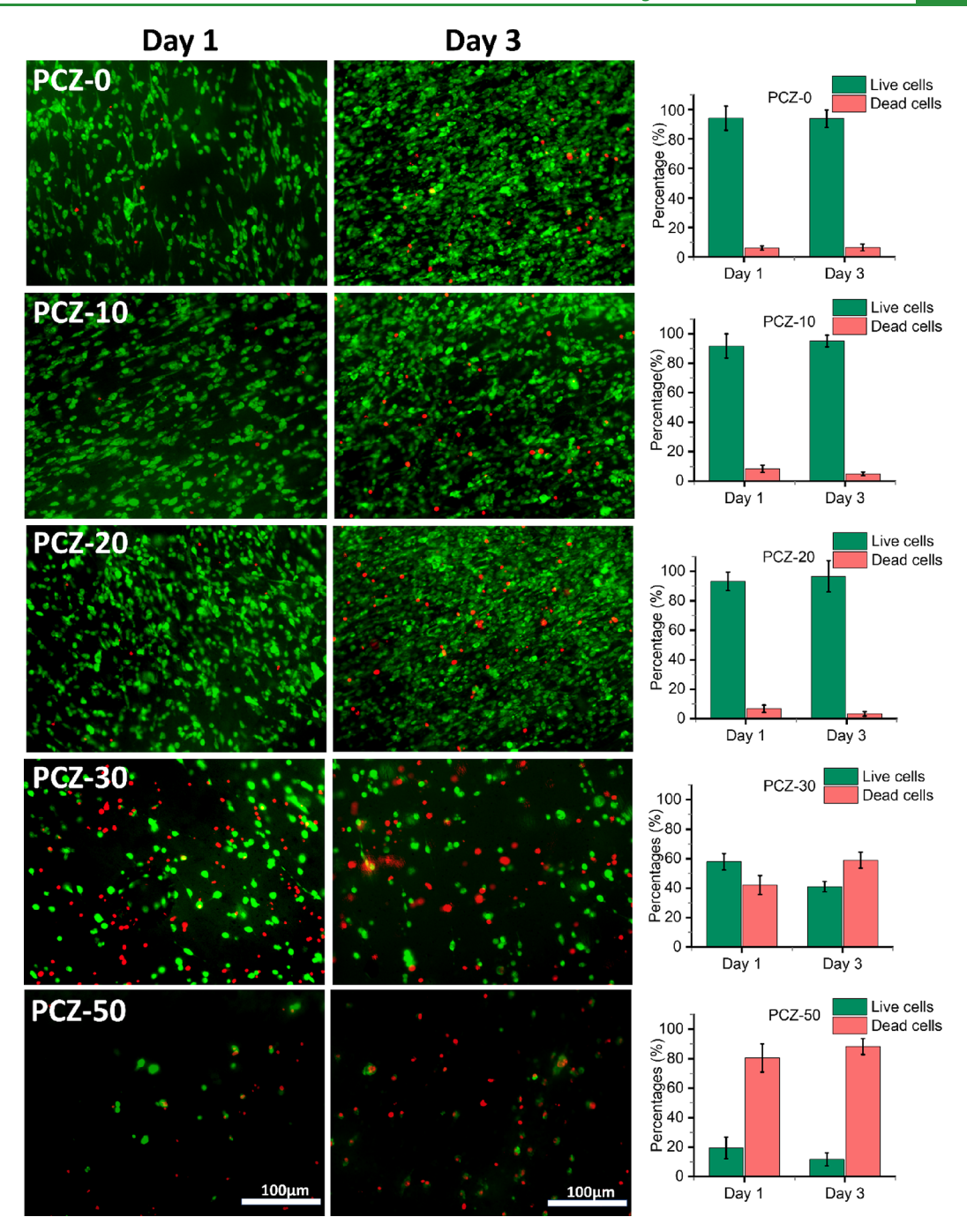


Figure 9. In vitro performance of the fibrous scaffold and effects on cell attachment and morphology. Fluorescence microscopy images represent live (stained green) and dead (stained red) NIH/3T3 fibroblasts cultured on the PCZ scaffolds for day 1 (left) and day 3 (right) utilizing acridine orange/propidium iodide dye (AOPI) (scale bar = 100 μ m). Right: Histograms show the counted percentage of live and dead cells in the corresponding fluorescent images using the ImageJ software (n = 5) of PCZ-0 to PCZ-50, respectively.

on the surface of the tissue culture plate (TCP) was flattened and polygonal shaped. The cytoskeleton outgrowth was observed as a well-distributed dendrite architecture, whereas the morphology was an elongated spindle-shaped cellular structure on the PZ and PCZ samples. In all samples, the cells are well-proliferated and well-spread. These results reveal that the morphology and the attachment of cells depend upon the orientation of the substrates used in culturing the cells.

Further evaluation of cellular compatibility, including cell attachment and spreading as well as cell—substrate interactions with PZ and PCZ fibers, was carried out by examining the cells

via SEM (Figure 11). Cells were attached strongly to the substrate with a successive cell proliferation. Cellular mass associated with elongated dendrites was observed. Notably, the cells were infiltrated into the PCZ scaffolds compared with PZ scaffolds. The cells were well-spread on the substrates, as shown in the representative images.

4. DISCUSSION

4.1. Characterization of the Morphology of Fibrous Scaffolds. To investigate the potential uses of PZ and PCZ fibers for biomedical applications, we first fabricated fibrous

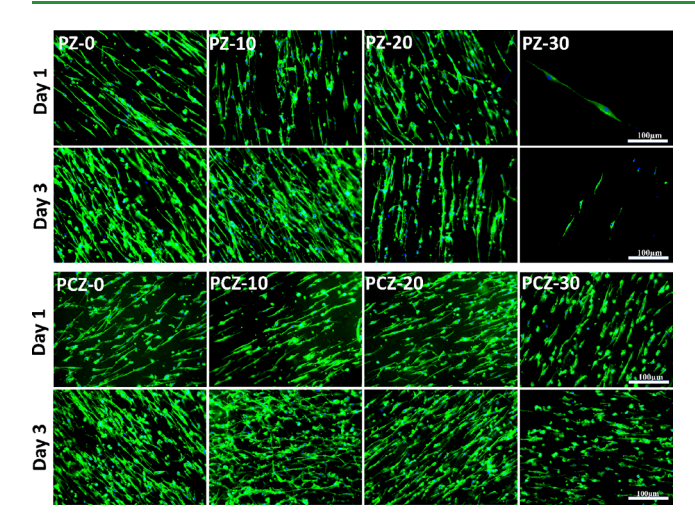


Figure 10. In vitro performance of scaffolds and their effects on cell morphology. Fluorescence microscopy images of NIH/3T3 cells cultured on PZ and PCZ fibrous scaffolds for day 1 and day 3. The cytoskeleton was stained with ActinGreen 488 (green), and the nuclei were counterstained with DAPI (blue) (scale bar = 100 μ m).

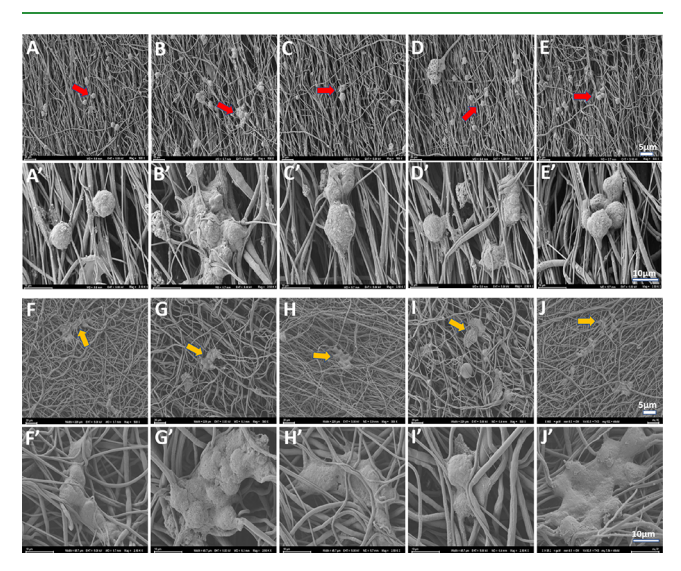


Figure 11. In vitro performance of scaffolds and effects on cell attachment and morphology. SEM images (A–E) represent the morphology and attachments of 3T3 fibroblasts cultured for 3 days on the scaffolds (PZ-0, PZ-10, PZ-20, PG-30, and PZ-50). Images A'–E' are high-resolution SEM images corresponding to A to E, respectively. SEM images (F–J) represent the morphology and attachments of 3T3 fibroblasts cultured for 3 days on the scaffolds (PCZ-0, PCZ-10, PCZ-20, PCZ-30, and PCZ-50). Images F'–J' are high-resolution SEM images corresponding to F–J, respectively.

scaffolds with varying amounts of Zn metal particles. Next, we analyzed their properties. Prior to their incorporation into the electrospinning solution, the as-received Zn particles underwent characterization including analysis of their shape, geometry, distribution, crystallinity, and hydrodynamic sizes. The hydrodynamic size of the Zn particles was found to be around 100 nm in number-weighted distribution and between 1000 and 10,000 nm in volume-weighted distribution. These numbers indicate that Zn was made up of a wide range of particle sizes with large aggregates of small particles, including small oxidized particles. The diffraction characteristics of the Zn particles matched those of Zn and ZnO.

The distribution of the Zn particles integrated into the individual fibers of the scaffolds was confirmed by elemental mapping via SEM-EDS and TEM analysis. TEM images further confirmed that Zn particles with diameters less than fiber diameters were well-encapsulated within the individual fiber regardless of being aggregated. One objective of the study was to determine the effect of Zn particles on the fiber diameter, surface area, and porosity of the scaffolds. The fibrous scaffolds without Zn (i.e., PZ-0 and PCZ-0) were used as a control. The analysis of the fiber diameter indicates that the diameter of both PZ and PCZ scaffolds ranged between 0.3 and 2.4 μ m. The average diameter of the PCZ fibers with increasing abundance of Zn particles was lower than the average diameters of the PZ fibers. Compared to the control fibers (i.e., PCZ-0), the fiber diameters of PCZ fibers were reduced significantly with increasing amount of Zn particles. This reduction might be because Zn particles were well-distributed in the PCL-CH solution and made the electrospinning solution more electrically conductive and caused the formation of thinner fibers. Because of the chelating nature of the CH, the surface of the Zn particles was coated with CH polymers, which helped them to distribute better in the PCL solution. The same conclusion could not be drawn with PZ fibers based on the discrepancies in the fiber diameter established. A higher percentage of heterogeneously sized Zn particles in the solution can result in fibers with a wide range of diameters. Additionally, metallic Zn particles can make the solution more conductive. Normally, the smaller metallic particles increase the charge density of the ejected jet during electrospinning, which increase the stretching of the jetted polymer solution, resulting in smaller diameter fibers. Instead, it is more likely that the greater numbers of larger-sized metal particles in the polymer solution contributed to larger fiber diameters by hindering this "jet stretching".

Scaffold materials for biomedical applications must be porous to promote cell adhesion and growth, as well as to exchange metabolites and cell nutrients. The pores of the scaffold also need to be interconnected to provide enough surface area for uniform cell distribution and facilitate the morphological patterning. The surface area and the porosity of the scaffolds were determined, and results showed that the Zn containing fibrous scaffolds produced larger surface areas compared to their controls, the non-Zn fibrous scaffolds, and also the more Zn containing scaffolds produced better surface area values. The porosity for the PZ and PCZ scaffolds ranged between 50 and 78%. This indicates that these scaffolds could be used to create a porous tissue engineering construct that mimics the fibrous ECM found in tissues⁵¹

4.2. Analysis of Chemical and Thermal Properties of Scaffolds. To determine if the presence of Zn particles altered the chemical and thermal properties of PZ and PCZ fibers, the scaffolds were studied using XRD, FTIR, DSC, and TGA. Two techniques, XRD and FTIR, were used to confirm the presence of Zn in the fiber. The results showed that the presence of Zn did not alter the chemistry of the PCL and PCL-CH fibers. The XRD patterns suggest that with different compositions of PZ and PCZ scaffolds, there was an increase in intensity corresponding to crystalline peaks of Zn and a decrease in intensity corresponding to crystalline peaks of the polymer. The XRD analysis also confirmed that Zn present in the scaffolds had the same crystalline phases as the Zn powder before electrospinning. However, both the X-ray diffraction

and FTIR spectra revealed that the presence of Zn did not alter the chemical structure of the PCL.

The thermal behavior of the scaffolds was examined by using TGA and DSC. The TGA results showed that all of the polymers burned completely at around 350 °C, leaving the Zn metal. The weight percent differences of each scaffold indicated in the TGA analysis were roughly close to the amount of Zn left in the scaffold after the polymer burned out. Additionally, the DSC results indicated that the presence of Zn did not significantly affect the melting characteristics of the scaffolds, regardless of the presence of Zn. The degree of crystallinity refers to the proportion of the polymer that exists in the crystalline form, and the crystallinity of PCL can be affected by various factors, including the presence of additives such as Zn. When Zn was added to PCL, it was likely to act as a nucleating agent, which means that it could promote the formation of new crystalline regions in the polymer. However, if the concentration of Zn is too high, then it can also interfere with the growth of these crystalline regions and inhibit their formation. Also, the increasing percentage of Zn particles can disrupt the alignment of the polymer chains in the crystalline regions, which can further reduce the crystallinity of the PCL. Zn may interact with the polymer chains and create defects or dislocations in the crystal structure, which can lead to a reduction in the degree of crystallinity as observed in the Supporting Information (Figure S2).

4.3. Mechanical Properties of PZ and PCZ Fibrous **Scaffolds.** The mechanical properties of the scaffold materials are essential to enhance decisions on needed materials because these materials undergo physicochemical changes in the body. Mechanical properties of a polymer composite are enhanced by the extent to which the fillers such as Zn particles become bonded to the polymer matrix and share in the load. This is sometimes difficult to determine more especially when each of these materials appears differently, that is, Zn being stiffer than the polymer matrix in this study. Polymeric scaffolds often become stiffer when hard particles such as metallic particles are added because of the reinforcing action. 52 It is a fact that fillers that are stiffer than the polymer matrix and have lower deformity and irregular shape can interfere with the alignment of the original matrix and can significantly alter the mechanical properties. Therefore, it is complex to predict the exact nature of the change in the mechanical properties of the composite scaffolds prepared by electrospinning. This is mostly due to the irregular distribution of the particles in the fiber. These results however were confirmed empirically⁵³ and are summarized in Tables 3 and 4 for this work.

Clearly, the addition of Zn regardless of the amount altered the mechanical properties of both the PZ and the PCZ scaffolds significantly. Overall, the presence of Zn made the fibrous scaffold more brittle, and the scaffold with the highest Zn (PZ-50 and PCZ-50) experienced the most brittleness. PZ-10 and PCZ-10 show a drastic increase in the Young's modulus and UTS as the Zn particles tend to reinforce the polymeric matrix. However, as the Zn concentration increases beyond a threshold, abrupt changes in the polymeric matrix occur, presenting discontinuities and lowering UTS as seen in several other composite fibers of PCL with metallic nanoparticles, including Mg, Ca, Zn, Fe, and so forth.²⁶⁻⁵⁴

The ductility of the samples was measured from the breaking strains and the highest strain needed for breakage, which was determined from the stress-strain curves and was significantly different across samples and scaffold types. Zn addition,

regardless of the amount, significantly altered the ductility of the scaffold. The highest ductility was observed in the PZ-0 and PCZ-0 samples. Deformity of a polymer results in an elastic response, but the availability of large irregular particles can stimulate inelastic developments that tend to affect the mechanical properties of the composites, including the Young's modulus, UTS, brittleness, and ductility. The possible way to further understand and predict how particles such as Zn affect mechanical properties of the scaffold will be when properties of each single fiber are analyzed and/or when particles with uniform size and shape are precisely distributed within the

4.4. Study of Zn Ion Release In Vitro. Zn²⁺ release plays a tremendous role in various cellular functions and is a key feature in the osteogenic differentiation of mesenchymal stem cells (MSCs)⁵⁵ as well as tissue healing activity. Zn particles are generally unstable in water and releases Zn2+ because of corrosion, and their corrosion appears worse in an electrolyte solution such as cell culture media. 56,57 As the PZ and PCZ scaffolds were incubated in cell media, Zn particles, loosely attached on top of the fiber surfaces and those embedded in the thin layers, had erosion started. After a short amount of time, water permeation started through the fiber matrix and allowed the Zn2+ to come out, which is a diffusion-controlled release. Zn²⁺ was then released into the surrounding media. To reduce the overexposure and overrelease of Zn²⁺, Zn particles are mostly encapsulated in the polymer matrix. PCL polymer is hydrophobic with a long linear aliphatic polyester structure that prevents fast water entry into the PCL bulk; as such, it slows down the rate of degradation.⁵⁸ It is well-known that having other additives, in our example, Zn particles and hydrophilic CH polymer, in the PCL alters the degradation rate of PCL scaffolds.⁵⁹ With increasing surface hydrophilicity and growing structural defects in PCL, the interaction of PCL molecules with water molecules does actually increase, which affects how quickly the scaffolds degrade. 60 The specific rate and the extent of release of Zn2+ from the PCL and Zn scaffolds are influenced by several factors, including the fabrication technique, Zn content, surface morphology, and degradation behavior of the composite 19

The concentration of Zn particles in the scaffold samples can significantly influence the release profile, with the higher Zn content generally leading to increased Zn²⁺ release.⁶¹ However, the release rate may reach a saturation point beyond a certain threshold concentration, where the release becomes more dependent on the degradation behavior of the polymer matrix. The scaffolds with a higher surface area-to-volume ratio enhanced ion release due to increased contact between the composite and the surrounding environment. A high surfaceto-volume ratio means high water penetration, which leads to high degradation rates⁶²

The degradation behavior of the polymer matrix can also determine the Zn release profile. PCL being a biodegradable polymer undergoes hydrolytic degradation, and its degradation rate can be tailored by adjusting its molecular weight, which in turn affects the Zn²⁺ release kinetics.³³

Changes in environmental factors such as pH, temperature, and the presence of other ions can affect the dissolution and diffusion of Zn2+ from the composite. For example, acidic conditions may accelerate the release of Zn2+, whereas the presence of certain ions may enhance or inhibit the release kinetics. Therefore, it is important to conduct comparative in

vitro release studies under identical conditions to accurately assess the relative release properties of the fibers.

Our results clearly indicated that a higher concentration of Zn²⁺ was released from the sample group PCZ than PZs when we compared the day-to-day release. The PCZ scaffolds released Zn²⁺ relatively faster and quantity-wise more than the PZ group. This can be explained by the presence of the chitosan in the PCL-CH group scaffolds. The hydrophilicity of chitosan is enhanced by the presence of NH₂ and OH groups along its chains, which speeds up the degradation of fiber by stimulating the free ions. The composite of PCL and CH exhibits higher hydrophilicity than the individual PCL fibers, which means that there is predictable water diffusion faster than the PZ fibers.

The standard deviations derived by summing variances each time point were used to conduct an ANOVA on the cumulative release after 336 h for two batches of both scaffold types. There was no batch difference represented between batches of the same scaffold (p < 0.001, n = 4). The highest amount of Zn²⁺ released was from the highest contained Zn particles for both groups. The amount of Zn²⁺ released by the PZ and PCZ was beyond the reported cytotoxic level, i.e., 150 mmol/L.⁴⁹ This release profile confirms that the Zn embedded PCL and PCL-CH scaffold is safe to use for tissue engineering and drug delivery application similar to the prior use of erythromycin-loaded poly(vinyl alcohol)-carboxymethyl cellulose/ZnO fibrous mat for drug delivery and wound dressing applications. 61 Our results also suggest, for future studies, that it might be possible to tailor the release of Zn²⁺ over a period of days to weeks by designing different thicknesses and geometries of fibers. Given that Zn2+ has multiple beneficial effects, it has a broad appeal for future biomedical applications.

4.5. Cytocompatibility In Vitro. 3T3 fibroblast cell viability and toxicity were analyzed via direct and indirect culturing on PZ and PCZ scaffolds utilizing the Alamar Blue assay and LDH assay up to day 3. For the direct cell culture study, more differences were observed on day 3 where viability for the PZ-30 and PZ-50 scaffolds dropped significantly to about half compared to their viability on day 1. For all the time points, PZ-10 and PZ-20 showed viability above the ISO standards (ISO-10993-5) that is 75%. 50 The PCZ scaffolds were not too different from the PZ because they also recorded a viability drop in PCZ-30 and PCZ-50 after day 3. This is because the cytotoxicity of Zn at low concentrations was significantly less in the dose-dependent response. In scaffolds with high concentrations of Zn, the particles could oxidize, forming ZnO, which is susceptible to generating reactive oxygen species (ROS). Consequently, the cells might be affected by the reactive oxygen stress. The release of Zn²⁺ that is 43.9 ppm from zinc chloride loaded on 3D spheroids for 24 h showed more than 50% cell viability with immortalized human oral keratinocytes (IHOKs). In contrast, only 4.8 ppm of Zn²⁺ was released from Zn chloride loaded on 2D scaffolds but showed similar results, suggesting that the release of Zn depends on the architecture and structural framework of the scaffolds that could also affect the cellular viability.⁶⁴ Furthermore, an vitro study reveals that the excess of \dot{Zn}^{2+} (>100 μ M) in serum-free media stimulates the function of monocytes to secrete proinflammatory cytokines but reduces the function of T cells by inhibition of the interleukin-1 receptor associated protein kinase. 65 Similarly, Zn2+ has been proven to improve cell viability of other types of cells such as osteoblasts between 1 and 50 μ M³⁴

Optimized Zn²⁺ into the substrate plays a central role for cellular Zn homeostasis in cell—substrate interaction, cellular migration, and gene expression, and but excessive Zn induced cellular toxicity including genetic disorder. Notably, there is always an optimal range of Zn²⁺ that supports many DNA binding proteins and allows chloride ions to cross the plasma membrane to maintain membrane potential.

The cell viability results from indirect cell culturing showed similar trends. For the indirect method, cells were directly exposed to the $\mathrm{Zn^{2+}}$ extract solution for 14 days. However, there was a massive viability recorded for both groups, especially PCZ scaffolds. PCZ-20 recorded the highest viability for days 1 and 3, possibly due to the presence of chitosan and a relatively safe amount of $\mathrm{Zn^{2+}}$ released. The toxicity release was much slower with the indirect method because the direct method was accompanied by the cells positioned on the fiber. The toxicity level of the indirect method could possibly be seen later after day 3 if investigated.

The bioactivity evaluation on the TCP, PZ, and PCZ samples seemed very interesting. Generally, cell adhesion and morphology are influenced by the architecture of the substrates, such as surface roughness, fiber orientation, and so forth. We observed a flat and broad cytoskeleton on the TCP, whereas on the PZ and PCZ samples, the cytoskeleton morphology of the cells was enlarged, elongated, and spindle shaped. The study explains that the structural behavior and development of the cell depend upon a specific niche in situ. These results demonstrate differences in cell behavior when the cells were cultured on the three different substrates. Further, the composite scaffolds containing chitosan appeared to be substantially higher and had better improvement in cellular growth and cell proliferation.

PCL has less cell recognition sites for being hydrophobic, and this however was improved by mixing with CH, which has a hydrophilicity effect and helps in good cell signaling response. Thus, micronutrient-rich bioscaffolds can be employed in tissue regenerative medicine and bioimplant materials that should have the ability to induce cell growth, proliferation, and spreading. Cellular activities are influenced by either the accumulation of intracellular Zn through exogenous administration or release from an intracellular Zn source, but the higher level of intracellular Zn concentration affects cellular apoptosis. The cell apoptosis by Zn is also associated with the activation of nicotinamide adenine dinucleotide phosphate (NADPH), a free-radical generating coenzyme that mediates with Zn and plays a crucial role to inhibit various antioxidant interventions. 66 Thus, the nanofibrous scaffold with enough porosity, hydrophilicity, and controlled mechanical property has excellent capability to mimic the natural microenvironment for cells and can easily promote the cellular activities in wound healing and tissue regeneration.

5. CONCLUSIONS

This research aimed to synthesize a novel Zn particle-composite biomaterial that has nanofibrous structural features and material properties that are beneficial for biomedical applications. Using an electrospinning technique, we designed and synthesized biodegradable PCL/Zn (i.e., PZ) and PCL-CH/Zn (i.e., PCZ) composite scaffolds with different concentrations of Zn particles. Various properties of the scaffolds were analyzed with the addition of Zn particles. The fiber morphology, crystallinity, thermal stability, mechanical

strengths, and biological properties of the scaffolds were very dependent on the amount of Zn particles embedded in the fibers. However, there was no change in the chemical structure of the PCL and PCL-CH fibers. In the Zn release experiment, the release of Zn²⁺ was proportional to the amount of Zn contained in the scaffold, where the highest amount released was from PZ-50 and PCZ-50 groups and the lowest amount was from PZ-10 and PCZ-10. Overall, the Zn²⁺ released from PCZ scaffolds was relatively higher and the release was faster compared to PZ fibers. Our viability results showed that scaffolds containing lower concentrations of Zn (i.e., PZ-10, PZ-20, PCZ-10, and PCZ-20) had no negative effect on the cells on days 1, 2, and 3. However, as the amount of Zn²⁺ increased in the release media, viability decreased with the higher Zn content scaffolds (PZ-30, PZ-50, PCZ-30, and PCZ-50). The cell viability, attachments, and cell morphology were improved when cultured with PCZ scaffolds. This proves that incorporation of chitosan changed the releasing kinetics of Zn²⁺ and helped to improve the cell response of the PCZ scaffolds. Hence, this newly developed biocompatible scaffold can be developed for a broad range of biomedical applications such as tissue engineering and wound healing applications as a scaffold with tunable material properties. As a continuation of our research, we hope to explore these scaffolds with more controllable physical and chemical properties to control the burst release of the particles upon immersion of the scaffolds in the culture media. The toxicity of the Zn-loaded scaffolds should be tested in animal models because in vivo systems are dynamic and more complex than in vitro conditions.

ASSOCIATED CONTENT

Supporting Information

The Supporting Information is available free of charge at https://pubs.acs.org/doi/10.1021/acsami.3c09793.

Preparation and visual observation of sedimentation of PCL/Zn solutions; Zn particle distribution study; surface morphology analysis; contact angle measurement and analysis; crystallinity of scaffolds; in vitro release study of Zn^{2+} ; and scaffold performance in vitro and effects on viability and toxicity of 3T3 cells using the indirect test method. (PDF)

AUTHOR INFORMATION

Corresponding Author

Narayan Bhattarai — Department of Chemical, Biological and Bioengineering and Center of Excellence in Product Design and Advanced Manufacturing, North Carolina A&T State University, Greensboro, North Carolina 27411, United States; orcid.org/0000-0002-0583-7913; Email: nbhattar@ncat.edu

Authors

Felix Tettey — Center of Excellence in Product Design and Advanced Manufacturing, Department of Chemical, Biological and Bioengineering, and Department of Industrial and Systems Engineering, North Carolina A&T State University, Greensboro, North Carolina 27411, United States

Sheikh Saudi – Department of Chemical, Biological and Bioengineering, North Carolina A&T State University, Greensboro, North Carolina 27411, United States

Dekonti Davies – Department of Chemical, Biological and Bioengineering and Department of Mechanical Engineering,

- North Carolina A&T State University, Greensboro, North Carolina 27411, United States
- Sita Shrestha Department of Chemical, Biological and Bioengineering, North Carolina A&T State University, Greensboro, North Carolina 27411, United States
- Kalene Johnson Department of Chemical, Biological and Bioengineering, North Carolina A&T State University, Greensboro, North Carolina 27411, United States
- Svitlana Fialkova Department of Mechanical Engineering, North Carolina A&T State University, Greensboro, North Carolina 27411, United States
- Kiran Subedi College of Agriculture and Environmental Sciences, North Carolina A&T State University, Greensboro, North Carolina 27411, United States
- Bishnu P. Bastakoti Department of Chemistry and Center of Excellence in Product Design and Advanced Manufacturing, North Carolina A&T State University, Greensboro, North Carolina 27411, United States; orcid.org/0000-0002-4651-7393
- Jagannathan Sankar Department of Mechanical Engineering and Center of Excellence in Product Design and Advanced Manufacturing, North Carolina A&T State University, Greensboro, North Carolina 27411, United States
- Salil Desai Department of Industrial and Systems
 Engineering and Center of Excellence in Product Design and
 Advanced Manufacturing, North Carolina A&T State
 University, Greensboro, North Carolina 27411, United
 States; Occid.org/0000-0002-6116-2105

Complete contact information is available at: https://pubs.acs.org/10.1021/acsami.3c09793

Author Contributions

 ${}^{
abla}$ F. Tettey and S. Saudi have an equal contribution.

Notes

The authors declare no competing financial interest.

ACKNOWLEDGMENTS

This work was supported financially by the National Science Foundation-Excellence in Research (NSF-EiR 2100861). Part of this research work was also supported by NSF-Engineering Research Centers (NSF-ERC 0812348 and 2133630) and by NSF-EiR 2100739, NSF-CMMI 1663128, and Center of Excellence in Product Design and Advanced Manufacturing (CEPDAM). We thank Dr. Udhab Adhikari, Dr. Shalil Khanal, Mr. Rabin Dahal, Dr. Kyle Nowlin, Dr. Bishnu K. Shrestha, Alexis Moody, and Elizabeth Martu for their technical assistance in research. Characterization of the fibers was also performed in part at the Joint School of Nanoscience and Nanoengineering, a member of the Southeastern Nanotechnology Infrastructure Corridor (SENIC) and the National Nanotechnology Coordinated Infrastructure (NNCI), which is supported by the National Science Foundation (NSF ECCS-1542174). The authors acknowledge the Analytical Services Laboratory at the College of Agriculture and Environmental Sciences, North Carolina A&T State University, for their valuable support in facilitating the sample preparation and elemental analysis.

REFERENCES

(1) Yang, H.; Jia, B.; Zhang, Z.; Qu, X.; Li, G.; Lin, W.; Zhu, D.; Dai, K.; Zheng, Y. Alloying Design of Biodegradable Zinc as Promising

- Bone Implants for Load-Bearing Applications. *Nat. Commun.* 2020, 11 (1), 401.
- (2) Lee, J. W.; Han, H. S.; Han, K. J.; Park, J.; Jeon, H.; Ok, M. R.; Seok, H. K.; Ahn, J. P.; Lee, K. E.; Lee, D. H.; Yang, S. J.; Cho, S. Y.; Cha, P. R.; Kwon, H.; Nam, T. H.; Han, J. H. L.; Rho, H. J.; Lee, K. S.; Kim, Y. C.; Mantovani, D. Long-Term Clinical Study and Multiscale Analysis of in Vivo Biodegradation Mechanism of Mg Alloy. *Proc. Natl. Acad. Sci. U.S.A.* **2016**, *113* (3), 716–721.
- (3) Yadav, K.; Sahu, K. K.; Sucheta; Gnanakani, S. P. E.; Sure, P.; Vijayalakshmi, R.; Sundar, V. D.; Sharma, V.; Antil, R.; Jha, M.; Minz, S.; Bagchi, A.; Pradhan, M. Biomedical Applications of Nanomaterials in the Advancement of Nucleic Acid Therapy: Mechanistic Challenges, Delivery Strategies, and Therapeutic Applications. *Int. J. Biol. Macromol.* 2023, 241, No. 124582.
- (4) Bowen, P. K.; Drelich, J.; Goldman, J. Zinc Exhibits Ideal Physiological Corrosion Behavior for Bioabsorbable Stents. *Adv. Mater.* **2013**, 25 (18), 2577–2582.
- (5) Mostaed, E.; Sikora-Jasinska, M.; Drelich, J. W.; Vedani, M. Zinc-Based Alloys for Degradable Vascular Stent Applications. *Acta Biomater.* **2018**, *71*, 1–23, DOI: 10.1016/j.actbio.2018.03.005.
- (6) Su, Y.; Cockerill, I.; Wang, Y.; Qin, Y.-X.; Chang, L.; Zheng, Y.; Zhu, D. Zinc-Based Biomaterials for Regeneration and Therapy. *Trends Biotechnol.* **2019**, 37 (4), 428–441, DOI: 10.1016/j.tib-tech.2018.10.009.
- (7) Hernández-Escobar, D.; Champagne, S.; Yilmazer, H.; Dikici, B.; Boehlert, C. J.; Hermawan, H. Current Status and Perspectives of Zinc-Based Absorbable Alloys for Biomedical Applications. *Acta Biomater.* **2019**, 97, 1–22, DOI: 10.1016/j.actbio.2019.07.034.
- (8) Mandal, A. K.; Katuwal, S.; Tettey, F.; Gupta, A.; Bhattarai, S.; Jaisi, S.; Bhandari, D. P.; Shah, A. K.; Bhattarai, N.; Parajuli, N. Current Research on Zinc Oxide Nanoparticles: Synthesis, Characterization, and Biomedical Applications. *Nanomaterials* **2022**, *12* (17), 3066.
- (9) Guillory, R. J., II; Kolesar, T. M.; Oliver, A. A.; Stuart, J. A.; Bocks, M. L.; Drelich, J. W.; Goldman, J. Zn2+-Dependent Suppression of Vascular Smooth Muscle Intimal Hyperplasia from Biodegradable Zinc Implants. *Mater. Sci. Eng.: C* **2020**, *111*, No. 110826.
- (10) Kambe, T.; Tsuji, T.; Hashimoto, A.; Itsumura, N. The Physiological, Biochemical, and Molecular Roles of Zinc Transporters in Zinc Homeostasis and Metabolism. *Physiol. Rev.* **2015**, *95*, 749–784, DOI: 10.1152/physrev.00035.2014.
- (11) Seo, H.-J.; Cho, Y.-E.; Kim, T.; Shin, H.-I.; Kwun, I.-S. Zinc May Increase Bone Formation through Stimulating Cell Proliferation, Alkaline Phosphatase Activity and Collagen Synthesis in Osteoblastic MC3T3-E1 Cells. *Nutr. Res. Pract.* **2010**, *4* (5), 356–361.
- (12) Chasapis, C. T.; Ntoupa, P.-S. A.; Spiliopoulou, C. A.; Stefanidou, M. E. Recent Aspects of the Effects of Zinc on Human Health. *Arch. Toxicol.* **2020**, *94*, 1443–1460.
- (13) Younus, H. Therapeutic Potentials of Superoxide Dismutase. *Int. J. Health Sci.* **2018**, *12* (3), 88.
- (14) Read, S. A.; Obeid, S.; Ahlenstiel, C.; Ahlenstiel, G. The Role of Zinc in Antiviral Immunity. *Adv. Nutr.* **2019**, *10* (4), 696–710.
- (15) Jiang, J.; Pi, J.; Cai, J. The Advancing of Zinc Oxide Nanoparticles for Biomedical Applications. *Bioinorg. Chem. Appl.* **2018**, 2018, 1062562 DOI: 10.1155/2018/1062562.
- (16) Lin, P.-H.; Sermersheim, M.; Li, H.; Lee, P. H. U.; Steinberg, S. M.; Ma, J. Zinc in Wound Healing Modulation. *Nutrients* **2018**, *10* (1), 16.
- (17) Qu, X.; Yang, H.; Yu, Z.; Jia, B.; Qiao, H.; Zheng, Y.; Dai, K. Serum Zinc Levels and Multiple Health Outcomes: Implications for Zinc-Based Biomaterials. *Bioact. Mater.* **2020**, *5* (2), 410–422.
- (18) Hess, S. Y.; Peerson, J. M.; King, J. C.; Brown, K. H. Use of Serum Zinc Concentration as an Indicator of Population Zinc Status. *Food Nutr. Bull.* **2007**, 28 (3), S403—S429.
- (19) Ferrone, E.; Araneo, R.; Notargiacomo, A.; Pea, M.; Rinaldi, A. ZnO Nanostructures and Electrospun ZnO-Polymeric Hybrid Nanomaterials in Biomedical, Health, and Sustainability Applications. *Nanomater* **2019**, *9* (10), 1449.

- (20) Törne, K.; Larsson, M.; Norlin, A.; Weissenrieder, J. Degradation of Zinc in Saline Solutions, Plasma, and Whole Blood. *J. Biomed. Mater. Res., Part B* **2016**, 104 (6), 1141–1151.
- (21) Bozym, R. A.; Chimienti, F.; Giblin, L. J.; Gross, G. W.; Korichneva, I.; Li, Y.; Libert, S.; Maret, W.; Parviz, M.; Frederickson, C. J.; Thompson, R. B. Free Zinc Ions Outside a Narrow Concentration Range Are Toxic to a Variety of Cells in Vitro. *Exp. Biol. Med.* **2010**, 235 (6), 741–750, DOI: 10.1258/ebm.2010.009258.
- (22) Ma, J.; Zhao, N.; Zhu, D. Endothelial Cellular Responses to Biodegradable Metal Zinc. ACS Biomater. Sci. Eng. 2015, 1 (11), 1174–1182.
- (23) Yamamoto, A.; Honma, R.; Sumita, M. Cytotoxicity Evaluation of 43 Metal Salts Using Murine Fibroblasts and Osteoblastic Cells. *J. Biomed. Mater. Res.* **1998**, 39 (2), 331–340.
- (24) Rijal, N. P.; Adhikari, U.; Khanal, S.; Pai, D.; Sankar, J.; Bhattarai, N. Magnesium Oxide-Poly (ε-Caprolactone)-Chitosan-Based Composite Nanofiber for Tissue Engineering Applications. *Mater. Sci. Eng.*: B **2018**, 228, 18–27.
- (25) Thompson, Z.; Rahman, S.; Yarmolenko, S.; Sankar, J.; Kumar, D.; Bhattarai, N. Fabrication and Characterization of Magnesium Ferrite-Based PCL/Aloe Vera Nanofibers. *Materials* **2017**, *10* (8), 937
- (26) Adhikari, U.; An, X.; Rijal, N.; Hopkins, T.; Khanal, S.; Chavez, T.; Tatu, R.; Sankar, J.; Little, K. J.; Hom, D. B.; Bhattarai, N.; Pixley, S. K. Embedding Magnesium Metallic Particles in Polycaprolactone Nanofiber Mesh Improves Applicability for Biomedical Applications. *Acta Biomater.* **2019**, 98, 215–234, DOI: 10.1016/j.actbio.2019.04.061.
- (27) Cifuentes, S. C.; Bensiamar, F.; Gallardo-Moreno, A. M.; Osswald, T. A.; González-Carrasco, J. L.; Benavente, R.; González-Martín, M. L.; García-Rey, E.; Vilaboa, N.; Saldaña, L. Incorporation of Mg Particles into PDLLA Regulates Mesenchymal Stem Cell and Macrophage Responses. *J. Biomed. Mater. Res. Part A* **2016**, *104* (4), 866–878.
- (28) Katarivas Levy, G.; Goldman, J.; Aghion, E. The Prospects of Zinc as a Structural Material for Biodegradable Implants—a Review Paper. *Metals* **2017**, *7* (10), 402.
- (29) Liu, Y.; Du, T.; Qiao, A.; Mu, Y.; Yang, H. Zinc-Based Biodegradable Materials for Orthopaedic Internal Fixation. *J. Funct. Biomater.* **2022**, *13* (4), 164.
- (30) MacEwan, M. R.; MacEwan, S.; Kovacs, T. R.; Batts, J. What Makes the Optimal Wound Healing Material? A Review of Current Science and Introduction of a Synthetic Nanofabricated Wound Care Scaffold. *Cureus* **2017**, *9* (10), No. e1736, DOI: 10.7759/cureus.1736.
- (31) Raina, N.; Pahwa, R.; Khosla, J. K.; Gupta, P. N.; Gupta, M. Polycaprolactone-Based Materials in Wound Healing Applications. *Polym. Bull.* **2021**, *79*, 1–23.
- (32) Edwards, A.; Jarvis, D.; Hopkins, T.; Pixley, S.; Bhattarai, N. Poly (E-caprolactone)/Keratin-based Composite Nanofibers for Biomedical Applications. *J. Biomed. Mater. Res. Part B* **2015**, *103* (1), 21–30.
- (33) Pulkkinen, M. Modified Poly (ε -Caprolactone) and Poly (Lactic Acid) Polymers for Controlled and Targeted Drug Delivery. University of Eastern Finland, Itä-Suomen yliopisto 2011.
- (34) Wang, S.; Gu, R.; Wang, F.; Zhao, X.; Yang, F.; Xu, Y.; Yan, F.; Zhu, Y.; Xia, D.; Liu, Y. 3D-Printed PCL/Zn Scaffolds for Bone Regeneration with a Dose-Dependent Effect on Osteogenesis and Osteoclastogenesis. *Mater. Today Bio* **2022**, *13*, No. 100202.
- (35) Harikrishnan, P.; Sivasamy, A. Preparation, Characterization of Electrospun Polycaprolactone-Nano Zinc Oxide Composite Scaffolds for Osteogenic Applications. *Nano-Struct. Nano-Objects* **2020**, 23, No. 100518.
- (36) Hasannasab, M.; Nourmohammadi, J.; Dehghan, M. M.; Ghaee, A. Immobilization of Bromelain and ZnO Nanoparticles on Silk Fibroin Nanofibers as an Antibacterial and Anti-Inflammatory Burn Dressing. *Int. J. Pharm.* **2021**, *610*, No. 121227, DOI: 10.1016/j.ijpharm.2021.121227.
- (37) Saudi, S.; Bhattarai, S. R.; Adhikari, U.; Khanal, S.; Sankar, J.; Aravamudhan, S.; Bhattarai, N. Nanonet-Nano Fiber Electrospun

- Mesh of PCL-Chitosan for Controlled and Extended Release of Diclofenac Sodium. *Nanoscale* **2020**, *12* (46), 23556–23569.
- (38) Bhattarai, N.; Li, Z.; Gunn, J.; Leung, M.; Cooper, A.; Edmondson, D.; Veiseh, O.; Chen, M. H.; Zhang, Y.; Ellenbogen, R. G.; Zhang, M. Natural-synthetic Polyblend Nanofibers for Biomedical Applications. *Adv. Mater.* **2009**, *21* (27), 2792–2797, DOI: 10.1002/adma.200802513.
- (39) Choong, L. T.; Yi, P.; Rutledge, G. C. Three-Dimensional Imaging of Electrospun Fiber Mats Using Confocal Laser Scanning Microscopy and Digital Image Analysis. *J. Mater. Sci.* **2015**, *50*, 3014–3030
- (40) Brown, A.; Zaky, S.; Ray, H., Jr; Sfeir, C. Porous Magnesium/ PLGA Composite Scaffolds for Enhanced Bone Regeneration Following Tooth Extraction. *Acta Biomater.* **2015**, *11*, 543–553.
- (41) Fischer, J.; Pröfrock, D.; Hort, N.; Willumeit, R.; Feyerabend, F. Reprint of: Improved Cytotoxicity Testing of Magnesium Materials. *Mater. Sci. Eng.: B* **2011**, *176* (20), 1773–1777.
- (42) Longhin, E. M.; El Yamani, N.; Rundén-Pran, E.; Dusinska, M. The Alamar Blue Assay in the Context of Safety Testing of Nanomaterials. *Front. Toxicol.* **2022**, *4*, No. 981701, DOI: 10.3389/ftox.2022.981701.
- (43) Tatum, S. D.; Saudi, S.; Tettey, F.; Bhandari, R. K.; Bhattarai, N. A NOVEL HYDROGEL-BRONCHIAL EPITHELIAL CELL SPHEROIDS FOR TOXICOLOGICAL EVALUATION. *Biomed. Sci. Instrum.* **2021**, *57*, 406–419.
- (44) Bastakoti, B. P.; Bhattarai, N.; Ashie, M. D.; Tettey, F.; Yusa, S.; Nakashima, K. Single-Micelle-Templated Synthesis of Hollow Barium Carbonate Nanoparticle for Drug Delivery. *Polymers* **2023**, *15* (7), 1739.
- (45) Qasim, I.; Mumtaz, M.; Nadeem, K.; Abbas, S. Q. Zinc Nanoparticles at Intercrystallite Sites of $(Cu_{0.5}Tl_{0.5})Ba_2Ca_3Cu_4O_{12-\delta}$ Superconductor. *J. Nanomater.* **2016**, 2016, 9781790 DOI: 10.1155/2016/9781790.
- (46) Vasireddi, R.; Javvaji, B.; Vardhan, H.; Mahapatra, D. R.; Hegde, G. M. Growth of Zinc Oxide Nanorod Structures: Pressure Controlled Hydrothermal Process and Growth Mechanism. *J. Mater. Sci.* **2017**, *52* (4), 2007–2020.
- (47) Muhammad, W.; Ullah, N.; Haroon, M.; Abbasi, B. H. Optical, Morphological and Biological Analysis of Zinc Oxide Nanoparticles (ZnO NPs) Using Papaver Somniferum L. *RSC Adv.* **2019**, 9 (51), 29541–29548.
- (48) Lee, K. H.; Kim, H. Y.; Khil, M. S.; Ra, Y. M.; Lee, D. R. Characterization of Nano-Structured Poly (ε -Caprolactone) Nonwoven Mats via Electrospinning. *Polymer* **2003**, *44* (4), 1287–1294.
- (49) Gren, M. S.; Mirastschijski, U. The Release of Zinc Ions from and Cytocompatibility of Two Zinc Oxide Dressings. *J. Wound Care* **2004**, *13* (9), 367–369.
- (50) Wang, J.; Witte, F.; Xi, T.; Zheng, Y.; Yang, K.; Yang, Y.; Zhao, D.; Meng, J.; Li, Y.; Li, W.; Chan, K.; Qin, L. Recommendation for Modifying Current Cytotoxicity Testing Standards for Biodegradable Magnesium-Based Materials. *Acta Biomater.* **2015**, *21*, 237–249.
- (51) Chong, E. J.; Phan, T. T.; Lim, I. J.; Zhang, Y. Z.; Bay, B. H.; Ramakrishna, S.; Lim, C. T. Evaluation of Electrospun PCL/Gelatin Nanofibrous Scaffold for Wound Healing and Layered Dermal Reconstitution. *Acta Biomater.* **2007**, *3* (3), 321–330, DOI: 10.1016/j.actbio.2007.01.002.
- (52) Tang, H.; Qi, C.; Bai, Y.; Niu, X.; Gu, X.; Fan, Y. Incorporation of Magnesium and Zinc Metallic Particles in PLGA Bi-Layered Membranes with Sequential Ion Release for Guided Bone Regeneration. ACS Biomater. Sci. Eng. 2023, 9, 3239 DOI: 10.1021/acsbiomaterials.3c00179.
- (53) Adams, J. M. Particle Size and Shape Effects in Materials Science: Examples from Polymer and Paper Systems. *Clay Miner.* **1993**, 28 (4), 509–530.
- (54) Boakye, M. A. D.; Rijal, N. P.; Adhikari, U.; Bhattarai, N. Fabrication and Characterization of Electrospun PCL-MgO-Keratin-Based Composite Nanofibers for Biomedical Applications. *Materials* **2015**, *8* (7), 4080–4095, DOI: 10.3390/ma8074080.

- (55) Park, K. H.; Choi, Y.; Yoon, D. S.; Lee, K.-M.; Kim, D.; Lee, J. W. Zinc Promotes Osteoblast Differentiation in Human Mesenchymal Stem Cells via Activation of the CAMP-PKA-CREB Signaling Pathway. *Stem Cells Dev.* **2018**, 27 (16), 1125–1135.
- (56) Zhang, E.; Yin, D.; Xu, L.; Yang, L.; Yang, K. Microstructure, Mechanical and Corrosion Properties and Biocompatibility of Mg—Zn—Mn Alloys for Biomedical Application. *Mater. Sci. Eng.: C* **2009**, 29 (3), 987–993.
- (57) Gu, X.; Zheng, Y.; Zhong, S.; Xi, T.; Wang, J.; Wang, W. Corrosion of, and Cellular Responses to Mg–Zn–Ca Bulk Metallic Glasses. *Biomaterials* **2010**, *31* (6), 1093–1103.
- (58) An, J.; Chua, C. K.; Leong, K. F.; Chen, C.-H.; Chen, J.-P. Solvent-Free Fabrication of Three Dimensionally Aligned Polycaprolactone Microfibers for Engineering of Anisotropic Tissues. *Biomed. Microdevices* **2012**, *14*, 863–872.
- (59) Mahdavi, R.; Belgheisi, G.; Haghbin-Nazarpak, M.; Omidi, M.; Khojasteh, A.; Solati-Hashjin, M. Bone Tissue Engineering Gelatin—Hydroxyapatite/Graphene Oxide Scaffolds with the Ability to Release Vitamin D: Fabrication, Characterization, and in Vitro Study. *J. Mater. Sci.: Mater. Med.* **2020**, 31, 1–14.
- (60) Díaz, E.; Sandonis, I.; Valle, M. B. In Vitro Degradation of Poly (Caprolactone)/NHA Composites. *J. Nanomater.* **2014**, 2014, No. 802435.
- (61) Darbasizadeh, B.; Fatahi, Y.; Feyzi-Barnaji, B.; Arabi, M.; Motasadizadeh, H.; Farhadnejad, H.; Moraffah, F.; Rabiee, N. Crosslinked-Polyvinyl Alcohol-Carboxymethyl Cellulose/ZnO Nanocomposite Fibrous Mats Containing Erythromycin (PVA-CMC/ZnO-EM): Fabrication, Characterization and in-Vitro Release and Anti-Bacterial Properties. *Int. J. Biol. Macromol.* **2019**, *141*, 1137—1146.
- (62) Ghorbani, M.; Nezhad-Mokhtari, P.; Ramazani, S. Aloe Vera-Loaded Nanofibrous Scaffold Based on Zein/Polycaprolactone/Collagen for Wound Healing. *Int. J. Biol. Macromol.* **2020**, *153*, 921–930.
- (63) Sun, H.; Mei, L.; Song, C.; Cui, X.; Wang, P. The in Vivo Degradation, Absorption and Excretion of PCL-Based Implant. *Biomaterials* **2006**, 27 (9), 1735–1740.
- (64) Lee, J.-H.; Lee, H.-H.; Kim, K.-N.; Kim, K.-M. Cytotoxicity and Anti-Inflammatory Effects of Zinc Ions and Eugenol during Setting of ZOE in Immortalized Human Oral Keratinocytes Grown as Three-Dimensional Spheroids. *Dent. Mater.* **2016**, 32 (5), e93—e104.
- (65) Wellinghausen, N.; Driessen, C.; Rink, L. Stimulation of Human Peripheral Blood Mononuclear Cells by Zinc and Related Cations. *Cytokine* **1996**, 8 (10), 767–771.
- (66) Zhang, C.; Sui, D.; Zhang, T.; Hu, J. Molecular Basis of Zinc-Dependent Endocytosis of Human ZIP4 Transceptor. *Cell Rep.* **2020**, 31 (4), No. 107582.